

LUT UNIVERSITY
LUT School of Energy Systems
LUT Mechanical Engineering

Atte Heiskanen

**DESIGN CASE FOR ADDITIVE MANUFACTURING: ELECTRODE FOR
ELECTROCHEMICAL GOLD SEPARATION PROCESS**

23.1.2020

Examiner(s): Docent Heidi Piili, D.Sc. (Tech.)

Advisor(s): Associate Professor Eveliina Repo, D.Sc. (Tech.)

Junior Research Scientist Markus Korpela, M.Sc. (Tech.)

TIIVISTELMÄ

LUT-Yliopisto
LUT School of Energy Systems
LUT Kone

Atte Heiskanen

Lisäävän valmistuksen suunnittelu -case: elektrodi sähkökemiallista kullanerotus prosessia varten

Diplomityö

2020

81 sivua, 39 kuvaa, 4 taulukkoa ja 1 liite

Tarkastajat: Dosentti Heidi Piili, TkT
Ohjaajat: Apulaisprofessori Eveliina Repo, TkT
Nuorempi tutkija Markus Korpela, DI

Hakusanat: AM suunnittelu, lisäävä valmistus, jauhepetisulatus, elektrodi, sähkökemialla, prosessisimulaatio

Tämän tutkimuksen tavoitteena oli tutkia ja ymmärtää laser pohjaisella jauhepetisulatuksella valmistettavien metallikomponenttien suunnitteluprosessia. Suunnitteluprosessia ja -työkaluja käytettiin sähkökemiallisessa kullan erotusprosessissa käytettävän elektrodin suunnitteluun. Työ koostuu kirjallisesta osasta, jossa tutkittiin suunnitteluprosessiin liittyviä mahdollisuuksia ja haasteita, ja case study -osasta, jossa elektrodi suunniteltiin.

Lisäävällä valmistuksella valmistettavien komponenttien suunnittelu on monitahoinen suunnittelun optimointiprosessi. Koska lisäävä valmistus tarjoaa merkittävää geometrista vapautta, suunnittelu on tärkeä tekijä, jolla osiin saadaan lisättyä arvoa, ja tätä kautta tehdä jauhepetisulatuksen käytöstä mahdollista. Valmistusprosessin rajoitteet ja mahdollisuudet on kuitenkin tärkeä ymmärtää. Lisäksi tarvitaan suunnittelutyökaluja, esimerkiksi topologiaoptimointia, verkkorakenteen luomista ja prosessisimulaatiota varten, jotta lisäävän valmistuksen tarjoamia suunnittelumahdollisuuksia voidaan hyödyntää.

Sähkökemiallisessa kullanerotusprosessia käytettävä elektrodi suunniteltiin hyödyntämällä kirjallisuusosuudessa tutkittuja suunnitteluprosessia ja -työkaluja. Tärkeimmiksi elektrodin toimintaan vaikuttaviksi tekijöiksi todettiin suuri pinta-ala ja tasalaatuinen huokoisuus. Nämä ominaisuudet saavutettiin hyödyntämällä tiheää verkkorakennetta kappaleen muodossa. Elektrodin valmistettavuutta laser pohjaisella jauhepetisulatuksella tarkasteltiin hyödyntämällä prosessisimulaatiotyökaluja. Simulaatioissa ei havaittu merkittäviä muodonmuutoksia, mikä viittaa siihen, että elektrodi on valmistettavissa ja käyttökelpoinen valmistuksen jälkeen. Jatkotutkimuksia vaaditaan, jotta käytettyjen simulointimenetelmien tulokset voidaan varmistaa ja elektrodin suorituskyky validoida.

ABSTRACT

LUT Univeristy
LUT School of Energy Systems
LUT Mechanical Engineering

Atte Heiskanen

Design case for additive manufacturing: Electrode for electrochemical gold separation process

Master's thesis

2020

81 pages, 39 figures, 4 tables and 1 appendix

Examiners: Docent Heidi Piili, D.Sc. (Tech.)

Advisors: Associate Professor Eveliina Repo, D.Sc. (Tech.)
Junior Research Scientist Markus Korpela, M.Sc. (Tech.)

Keywords: design for additive manufacturing, additive manufacturing, powder bed fusion, electrode, electrochemistry, process simulation

The aim of this thesis was to study and understand the design process of metallic components to be manufactured with laser-based powder bed fusion (L-PBF). The design process and tools were applied to design an electrode used in electrochemical gold separation process. The thesis was done by conducting literature review to understand the possibilities and challenges related to this process, and case study, where the electrode was designed.

Design of additively manufactured components is multifaceted design optimization process. As the additive manufacturing offers significant geometrical freedom, design is an important factor to add value to parts, to make the use of L-PBF feasible. However, the possibilities and limitations of the manufacturing process need to be well understood. Additionally, various design tools, such as topology optimization, lattice generation and build process simulation software, are required to fully leverage the design possibilities offered by AM.

Electrode structure to be used in electrochemical gold separation process was designed by applying the design process and tools studied in the literature part. Most important factors for the electrode design were deemed to be the surface area and uniform porosity. These were achieved by using very fine lattice structure. Manufacturability of the electrode via L-PBF was then studied by conducting build process simulations, where no significant deformations were observed, suggesting that the electrode design would be manufacturable and usable after build process. Further studies are required to confirm the results of used simulation methods and to validate the electrode performance.

ACKNOWLEDGEMENTS

The thesis was done in the research group of Laser Material Processing and Additive Manufacturing of LUT University as a part of ReGold-AM project funded by Academy of Finland. The project and this thesis are carried out in co-operation with research group of Hydrometallurgy for Urban Mining. The aim of the project is to construct novel electrochemical reactors for gold recovery purposes by leveraging possibilities offered by AM. The project will last from 01.09.2019 to 31.08.2023. I would like to thank the support of the project and project partners for making this thesis possible.

I would also like to express my gratitude to my thesis advisors Docent Heidi Piili, Associate Professor Eveliina Repo and Junior Research Scientist Markus Korpela for providing help and advices whenever needed.

Additionally, thanks to my family, especially my spouse Eve, for their support and encouragement during this thesis and throughout my studies.

Atte Heiskanen

Atte Heiskanen

Lappeenranta 23.1.2020

TABLE OF CONTENTS

TIIVISTELMÄ

ABSTRACT

ACKNOWLEDGEMENTS

TABLE OF CONTENTS

LIST OF SYMBOLS AND ABBREVIATIONS

1	INTRODUCTION	9
	1.1 Background	9
	1.2 Aim and framing of the research	10
2	DESIGN FOR ADDITIVE MANUFACTURING	11
	2.1 DfAM process	14
	2.2 Design optimization	16
	2.2.1 Topology optimization	16
	2.2.2 Lattice structures	18
	2.2.3 Fluid flow optimization	20
	2.2.4 Part consolidation	21
	2.3 Additional design considerations	22
	2.3.1 Support structures and build orientation	22
	2.3.2 Residual stresses	24
	2.3.3 Material properties	27
	2.3.4 Problems in DfAM	29
3	BUILD PROCESS SIMULATION	30
	3.1 Inherent strain approach	31
	3.2 Thermo-mechanical methods	33
4	CASE STUDY: ADDITIVELY MANUFACTURED ELECTRODE	44
	4.1 Application of the electrochemical process	44
	4.2 Additively manufactured electrodes	46
	4.3 Factors affecting electrode performance	49
	4.3.1 Geometrical factors	49
	4.3.2 Material factors	53
5	DESIGN PROCESS OF THE ELECTRODE	54

5.1	Defining requirements	54
5.2	Material choice	55
5.3	Modeling.....	56
5.4	Simulation.....	57
5.4.1	Thermo-mechanical simulation	57
5.4.2	Inherent strain analysis	61
6	RESULTS AND DISCUSSION	63
6.1	DfAM process.....	63
6.2	Electrode design.....	64
6.3	Build process simulations	65
6.3.1	Thermo-mechanical simulation	66
6.3.2	Inherent strain simulation	67
6.3.3	Discussion.....	69
7	CONCLUSIONS	71
8	FURTHER STUDIES.....	74
	LIST OF REFERENCES.....	75
	APPENDIX	

Appendix I: Material properties of 316L used for thermo-mechanical simulation.

LIST OF SYMBOLS AND ABBREVIATIONS

α	Thermal expansion coefficient
ε	Emissivity
ε_e	Elastic strain
ε_{pl}	Plastic strain
ε_{th}	Thermal strain
σ	Stefan-Boltzmann constant
σ	Stress
σ_{comp}	Compressive stress
σ_{tens}	Tensile stress
ρ	Density
A	Electroactive area
A_e	Electroactive area of the electrode per unit volume
C	Specific heat capacity
h	Heat transfer coefficient
k	Thermal conductivity
k_m	Mass transfer coefficient
Q	Internal heat generation
q_{conv}	Heat transfer due to convection
q_{rad}	Heat transfer due to radiation
T_0	Ambient temperature
ΔT	Temperature change
v	Mean linear flow velocity
V_e	Electrode volume
X_A	Fractional conversion
AM	Additive manufacturing
Cr	Chromium
DfAM	Design for Additive Manufacturing
FE	Finite element

FEA	Finite element analysis
FEM	Finite element method
HIP	Hot isostatic pressing
ISO	International Organization for Standardization
L-PBF	Laser-based powder bed fusion
Mo	Molybdenum
PBF	Powder bed fusion
TO	Topology optimization

1 INTRODUCTION

Additive manufacturing (AM) is a manufacturing method, of which use has increased considerably in recent years (Wohlers et al. 2019, p. 169). Multiple different methods can be considered AM, with all manufacturing parts by adding material (SFS-EN ISO/ASTM 52900:en 2017, p. 8). This makes AM inherently different to more traditional manufacturing methods, and thus new aspects need to be considered from design perspective as well (Wohlers et al. 2019, p. 212).

1.1 Background

Laser-based powder bed fusion (L-PBF) is the most widely adopted metal AM method (Milewski 2017, p. 37; Yang et al. 2017, p. 63). It can be used to manufacture metallic parts with increased complexity, but the process also has its limitations (Wohlers et al. 2019, p. 173). Therefore, the designing and manufacturing of AM parts require understanding of both limitations and possibilities of the manufacturing method. Multitude of design rules and tools have been developed especially for this purpose and can be leveraged to design highly optimized parts for variety of applications. (Diegel et al. 2019, p. 121.)

A possible field benefitting from geometrical freedom is electrochemistry, as electrodes can be designed with more freedom to increase the efficiency of electrochemical processes (Arenas et al. 2017, p. 133). One application of electrochemical process is gold recovery from electronic waste (Kim et al. 2011, pp. 207–208). As the economic growth and technological advances have resulted in the increase of electronic waste, this process has generated interest. The waste contains high quantity of gold, with concentrations of 100 times higher than generally found in gold ore. (Kim et al. 2011, p. 206) The process relies on electrodes, which can benefit from complex geometrical features (Arenas et al. 2017, p. 133).

The challenges related to design of AM parts and their application to design of electrodes form the research problem of this thesis. The design process and the possibility to design electrodes with optimal geometries to be manufactured via L-PBF are studied.

The thesis was carried out in the research group of Laser Material Processing and Additive Manufacturing of LUT University as a part of ReGold-AM project funded by Academy of Finland. The project is done in co-operation with research group of Hydrometallurgy for Urban Mining. The aim of the project is to construct novel electrochemical reactors for gold recovery purposes by leveraging possibilities offered by AM. The project lasts from 01.09.2019 to 31.08.2023.

1.2 Aim and framing of the research

Motivation for this thesis was to determine challenges and possibilities related to the process of designing parts to be manufactured with L-PBF. As the manufacturing method differs inherently from traditional methods, new design approaches need to be adopted (Wohlers et al. 2019, p. 212). The aim of the thesis can be summed to following questions:

- Which kind of design process has to be used for additively manufactured components?
- Which design tools are used in the design of additively manufactured components?
- How can these design possibilities be used in the design of electrodes?

Thesis consists of literature review and case study part. In the literature review, design process and tools for additively manufactured components are visited in detail, using scientific articles and literature as reference. The collected information is used to determine what is the design process for AM, which design tools are required and what needs to be taken into consideration when designing for AM.

The case study focuses on the design of electrodes used in electrochemical gold recovery process. The design aspects studied within literature review are applied in the case to demonstrate the design process of AM parts and to successfully design an additively manufacturable electrode. Hypothesis is that by considering AM design aspects, optimized electrode structure can be designed.

While in this thesis, the design tools and process are applied to design electrodes to improve electrochemical gold recovery process, it also provides comprehensive information about design for AM that can be used across a variety of industries.

2 DESIGN FOR ADDITIVE MANUFACTURING

Traditional subtractive manufacturing has significant constraints on the types of geometries that can be produced. Therefore, products with simple geometries are preferred on the cost of performance. Additive manufacturing, while also having some limitations, allows the production of products with much higher degree of complexity. Design freedom can be leveraged to design products with optimized performance and functionality. (Yang & Zhao 2015, p. 327–330.) An example of optimized part is presented in Figure 1.



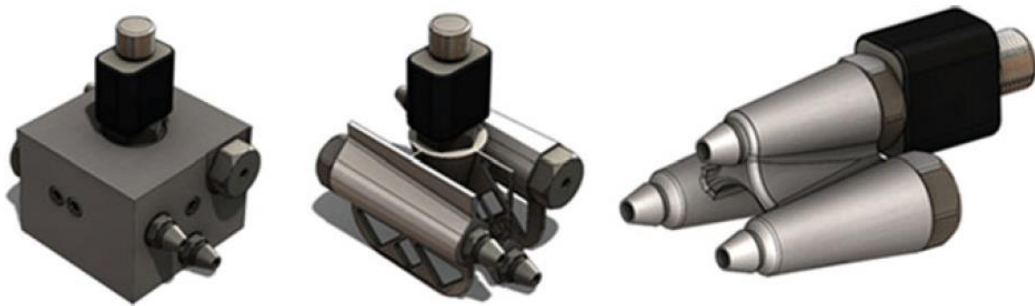
Figure 1. A gas emission rake designed and optimized for additive manufacturing. Geometry cannot be manufactured with traditional methods, shapes are optimized, and multiple parts are consolidated into one. (Diegel et al. 2019, p. 133.)

As it can be seen from Figure 1, optimization of multiple properties is possible within the same part. This can be done for example to reduce weight, lower stress concentrations, enhance flow properties and consolidate parts (Diegel et al. 2019, p. 133; Yang & Zhao 2015, p. 327–330.)

Design for Additive Manufacturing (DfAM) is a design approach, which exploits the possibilities of AM technologies, while simultaneously considering its constraints and

limitations. As geometries can be designed with more freedom, functional performance and other key product considerations can be set as priority within the design process. This is in stark contrast to traditional design approaches, where the manufacturing process requirements are the key factors driving the design process. Because of this difference, DfAM requires radical change in the mindset of designer. (Wohlers et al. 2019, p. 212.)

Additive manufacturing is expensive and slow manufacturing method compared to traditional ones. Therefore, the implementation of DfAM is critical for the justification of the use of AM. In general, parts not specifically designed for AM are not worth manufacturing with the technology. Diegel et al. (2019) divide additively manufactured parts into three categories, presented in Figure 2. (Diegel et al. 2019, pp. 41–42; pp. 132–133.)



Direct part replacement	Adapt for Am	Design for AM
4.6 kg	1.0 kg 78% weight saving.	0.4 kg 91% weight saving. Improved fluid flow and fit within product. Less space required in product, and easier assembly.

Figure 2. Three categories of DfAM (Diegel et al. 2019, p. 42).

First category presented in Figure 2 is direct replacement parts, where part needs to be additively reproduced very closely to existing part manufactured with traditional methods. This is mainly seen in some spare part applications, where the use of AM can be justified for example with lead time considerations. In this category, only the build process of the part is considered in the design. Second category is parts adapted for AM. In this category, some

changes are made to the original part internally and externally to improve its performance and manufacturability. Its use and function still remain the same. In third category, the entire part is designed from AM perspective to maximize its benefits. In this category the part performance, function and fit to its surroundings are all reconsidered and improved. Cases like this justify the use of AM best, as it can add significant value over traditional manufacturing methods. (Diegel et al. 2019, pp. 41–42; pp. 132–133.)

In addition, the design has a direct effect on the build time and post-processing needs. Main L-PBF process steps are presented in Table 1. The steps for which the total build times are affected by the design are highlighted. (Wohlers et al. 2019, pp. 221–225; pp. 244–245.)

Table 1. L-PBF process steps and the steps which effect on build time can be affected by design. (Modified from Wohlers et al. 2019, p. 223).

L-PBF process step	Build time affected by design
Pre-processing and printing	
Clean the AM system	no
Purge the system of oxygen	no
Preheat the AM system	no
Recoating	no
Melt contour lines	yes
Melt interior hatch patterns	yes
Build platform removal	no
Powder recycling	no
Post-processing	
Thermal stress relief	yes
Part removal from build platform	no
Hot isostatic pressing	no
Support structure removal	yes
Heat treatment	yes
Shot peening, surface machining etc.	no
Inspection	no

As it can be seen from Table 1, the design choices have an impact on several steps affecting the total build time, the most important being the amount of powder needed to be melted. This can be affected by design practices. For example, minimizing large volumes of solid material will decrease time that laser needs to scan back and forth. This same choice will

also have effect on the need for thermal stress relief, as mostly uniform wall thicknesses will contain lesser residual stresses from the build process. Additional general design rules and solutions are visited in more detail in the following chapters. (Wohlers et al. 2019, pp. 223–224.)

2.1 DfAM process

DfAM is a design optimization process, in which objective functions are maximized, while respecting the constraints. This is done iteratively by altering design variables to come up with the optimal design. The structural optimization objectives can vary from the optimization of stiffness and strength to thermal and biomedical applications. Therefore, the implementation of this approach requires competence in number of fields, as understanding of different functional, manufacturing and aesthetic requirements need to be taken into account. To achieve the design goals, tools such as advanced computer-aided design (CAD) and finite element analysis (FEA) are used with the consideration of design rules that are determined by the manufacturing process. (Gebisa & Lemu 2017, p. 727; Graziosi et al. 2017, p. 1544; Yang & Zhao 2015, p. 335.)

Orqu era et al. (2017) have recognized six steps as the main phases of DfAM process (Orqu era et al 2017, p. 223):

1. Requirements analysis
2. Structural optimization
3. Interpretation of results
4. Rendering
5. Finite element analysis
6. Final design

Following these steps, requirements and objectives for the design are first determined after which an optimization process is performed. The results are interpreted, and the design is realized to CAD format based on them. After this, finite element analysis is done to validate that the part fulfills the requirements. If validation is successful, final design is then achieved. (Orqu era et al. 2017, pp. 223–226.)

Similar DfAM process structure has been proposed by Yang & Zhao (2015). In this structure, the process is divided into two main steps based on the initial input of the design model. The process structure is presented in Figure 3. (Yang & Zhao 2015, p. 339.)

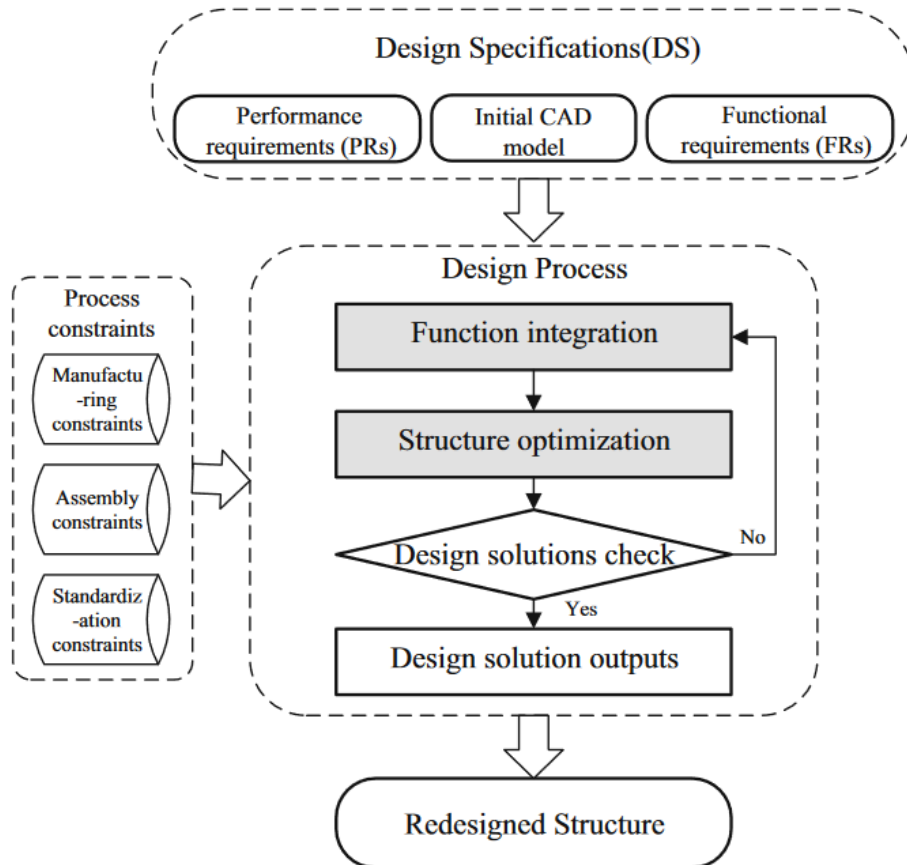


Figure 3. DfAM process structure (Yang & Zhang 2015, p. 339).

In the Figure 3, the two main steps are function integration and structure optimization. The former is accomplished by analyzing initial CAD model and performing any possible function integration procedures, such as part consolidation, based on performance and functional requirements. In the latter main step, structure optimization methods are applied on this newly created design space. This is done to increase performance, such as lighter weight or better heat conduction properties. These two steps will also need to comply with process constraints, as presented on the left in Figure 3. The design solution is then validated and if any problems occur, design flow goes back to the first step for modifications. If validation is successful, optimal part design is achieved based on solution outputs. (Yang & Zhao 2015, p. 338–339.)

2.2 Design optimization

Several methods and tools within DfAM can be used to optimize the structure and add value to the part. Available methods are handled in detail in this chapter.

2.2.1 Topology optimization

Excess material in part produced with additive manufacturing will increase its production time and costs. In addition, light weighting can add significant value in for example aerospace and transportation applications, where even small decreases in weight can lead to savings (Wohlers et al. 2019, p. 216). Therefore, topology optimization (TO) has been recognized as one of the key tools for structural optimization. TO allows the design of parts with reduced material, while retaining similar functional specifications as conventional parts. Manufacturing of this kind of optimized parts has been made feasible by the geometrical freedom provided by AM technologies. (Wohlers et al. 2019, p. 216.)

TO is an algorithm-based mathematical tool, which optimizes the material distribution within a given design space. Optimization is based on specifically defined objective. This objective can for example be minimizing or maximizing part property, such as weight, stiffness or resonant frequency. This is done by applying finite element (FE) method, where the model is divided into elements. During the optimization, these elements are assigned density values and are selectively removed or added based on it. The resulting structure is checked against the target objective and optimization is done iteratively until satisfactory result is achieved. Several different algorithms for TO exists, but the process remain quite the same. (Yang et al. 2017, pp. 122–127.) Workflow for TO is presented in Figure 4.

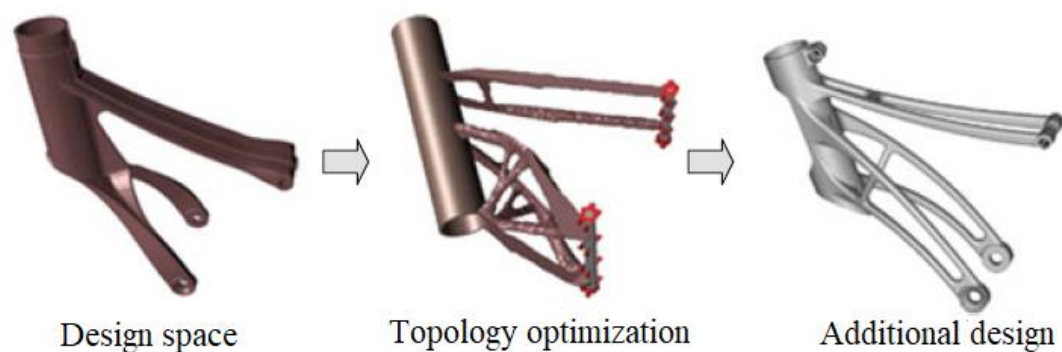


Figure 4. Topology optimization workflow (Modified from Yang et al. 2017, p. 126).

As it can be observed from Figure 4, TO workflow begins by defining optimization goals and the available design space. Traditionally designed part can be used as the design space, if one exists. However, it is often good practice to simplify and add material around the part with respect to surrounding assembly pieces and fixturing. Functional regions within the design space are then defined. Functional areas can be for example bolt holes or contact surfaces, areas where loads and boundary conditions are applied or other critical part features. During the optimization, material is not removed from these areas. Design space is then meshed to FEA model and appropriate loading and boundary conditions are set. It is important to consider all the potential loading conditions to properly capture necessary stress states. (McKee & Porter 2017, pp. 55–58.) The effect of considering multiple stress states versus only one is presented in Figure 5.

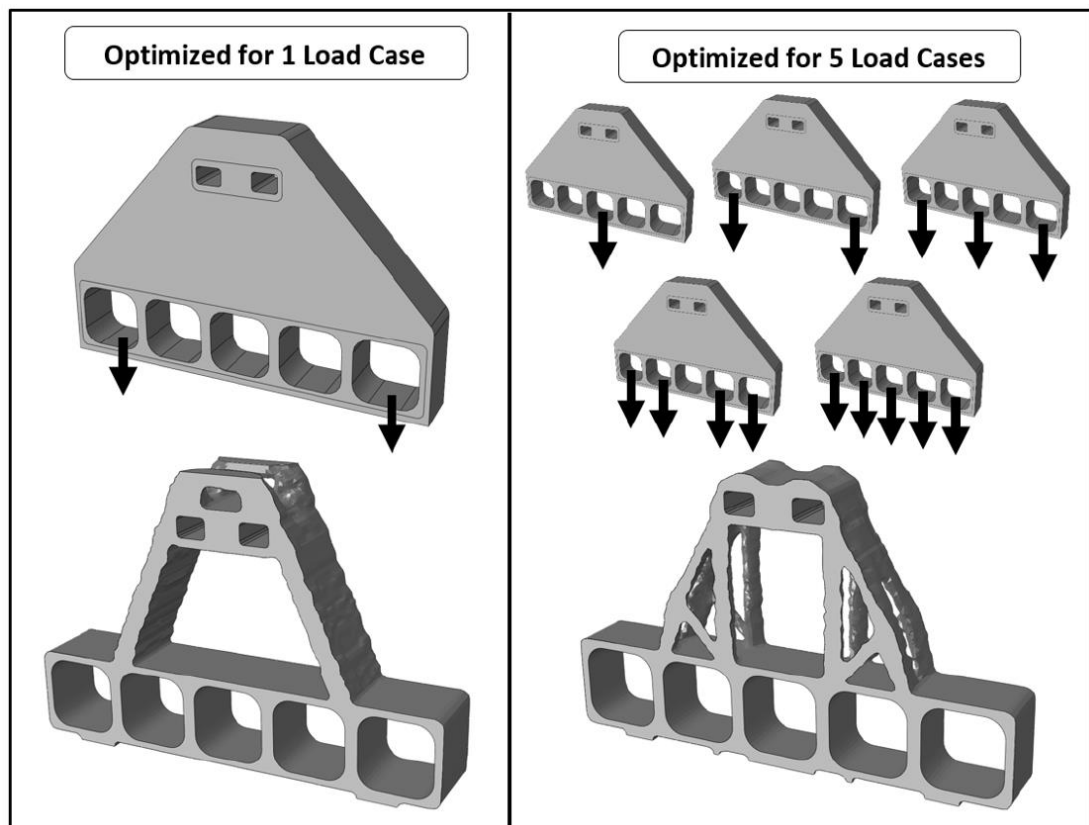


Figure 5. Topologically optimized hanger for one (left) and five (right) potential loading cases (McKee & Porter 2017, p. 57).

As it can be seen from Figure 5, the determination of load cases has effect on optimized geometry. Geometry can also be affected by additional optimization constraints. Geometry constraints, such as determining minimum wall thicknesses or overhang angles can also be defined during the TO setup. (McKee & Porter 2017, pp. 55–58.)

Once the FEA model is established, TO algorithm can be ran. Based on algorithm and amount of constraints, process will require tens to hundreds of iteration cycles (McKee & Porter 2017, p. 61). Output from TO is often not suitable for production as is. Although some FE mesh editors can automatically rebuild and smooth the geometry, additional manual design and verification is often required to achieve functionally and aesthetically satisfactory design and to enable later modification of the model. (Diegel et al. 2019, pp. 75–76.)

2.2.2 Lattice structures

Another option to reduce the mass of an additively manufactured part is through the use of lattice structures. Lattice structures consist of small specifically specified cells with certain shape, size, and thickness. These cells are used to replace solid material in part and to increase its strength and rigidity. Depending on application, entire part volume can be converted to lattice structure or leave its outer shell or connection points to solid, while converting only certain areas. (Diegel et al. 2019, pp. 134–135.) Example of lattice structure used within a part is presented in Figure 6.



Figure 6. Lattice structure used within a part. Volume around connection points is left solid. (Modified from nTopology 2019a.)

As it can be seen from Figure 6, lattice structures can be optimized similarly to topology optimization. In this method, lattice strut thicknesses and cell sizes are varied within the structure. The thickness and size values for each cell are determined based on FEA results. Denser and thicker lattices are used in highly stressed areas and vice versa. In addition, TO and lattice size optimization can in some cases be combined to achieve greater weight reductions. (Diegel et al. 2019, p. 76; Gibson et al. 2015, p. 429.)

In addition to weight reduction, lattice structures can also be used for other functions. Energy absorption, thermal conductivity and vibration dampening have all been recognized as properties that can be enhanced with the use of lattices. Additionally, lattice structures have been widely adapted for medical applications. (Gibson et al. 2015, p. 415; Gu 2015, p. 8; Wohlers et al. 2019, p. 218.) Medical application parts with lattice structure are presented Figure 7.

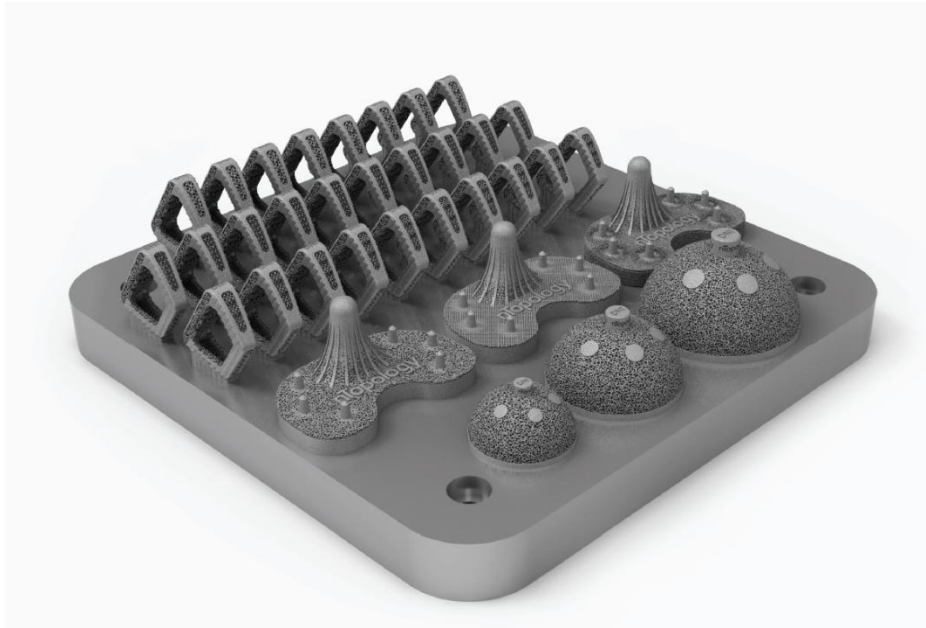


Figure 7. Lattice structure utilized in medical applications (nTopology 2019b).

In Figure 7, lattice structure is utilized on medical implants. The porous nature of these structures can be used to reduce body rejection of the implant, as it closely mimics the structure of actual bones. This in combination with lighter weight and customization possibilities offered by AM, can be very beneficial in prosthetic implants. (Gu 2015, p. 8; Milewski 2017, p. 191; Wohlers et al. 2019, p. 218.)

Minimum feature sizes and cell shape should be considered in the design of lattice structures. Theoretical minimum strut thickness manufacturable with L-PBF systems would be around 0.15 mm but struts this small would have very limited strength and fatigue resistance. A sensible minimum strut thickness would be 0.5–1 mm. The cell shape should be designed to be self-supporting to avoid the need of support structure removal from very small features. (Diegel et al. 2019, p. 137–138.)

2.2.3 Fluid flow optimization

Gas and liquid are highly sensitive to shapes of the part they are flowing on. When designing for additive manufacturing, flow features can be designed to be closer to optimal shapes than with traditional manufacturing methods, thus enhancing flow efficiency. (Wohlers et al. 2019, p. 218.) Cooling channels have traditionally been drilled on parts, which has limited their use and compromised efficiency. Additive manufacturing allows the design of

conformal cooling channels integrated into parts, as presented in Figure 8. (Diegel et al. 219, pp. 87–88; Milewski 2017, pp. 21–22; Wohlers et al. 2019, pp. 218–219.)

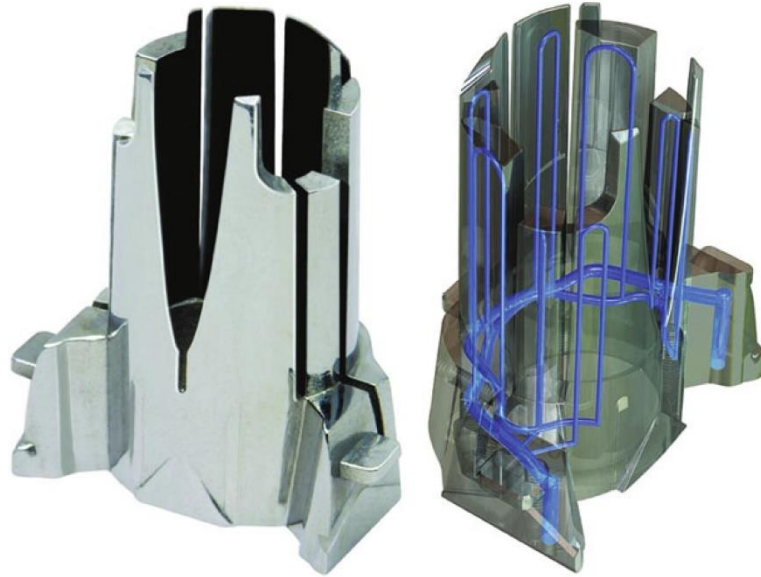


Figure 8. Additively manufactured part on right with its conformal cooling channels highlighted on left (Milewski 2017, p. 22).

As it can be seen from Figure 8, channels can be designed for optimal coolant flow. These can be used in multiple applications across the industrial sector, being very effective in high temperature applications like turbine blades and combustion chambers. Integrated and optimized cooling channels are also used in injection molding molds to improve cooling process and shorten cycle times. (Diegel et al. 219, pp. 87–88; Milewski 2017, pp. 21–22; Wohlers et al. 2019, pp. 218–219.)

2.2.4 Part consolidation

Additive manufacturing allows parts that are traditionally made from multiple single parts to be designed as one more complex part in some cases. When designing for AM, it is good practice to consider surrounding assembly parts and the possibility to combine them. (Diegel et al. 219, p. 79; ISO/ASTM 52910 2018, p. 9; Wohlers et al. 2019, p. 234.) An example of part consolidation is presented in Figure 9.

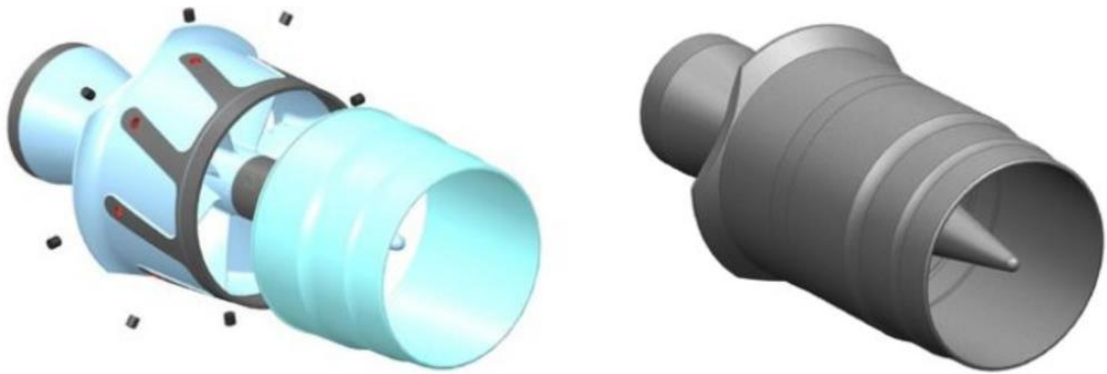


Figure 9. Multi-parts assembly combined to one additively manufactured part (Huff & Wohlers 2019, p. 172).

As it can be seen from Figure 9, the utilization of part consolidation can eliminate the need for fasteners and assembly. This alone can justify the use of AM, as supply chain overhead, labor and other costs related to assembly are reduced. The need for tight tolerances is also affected, as parts needed to fit together are manufactured as one. (Diegel et al. 2019, pp. 79–81.)

2.3 Additional design considerations

Additional important aspects should be considered during the DfAM process. These aspects include geometry, material property and process considerations and are handled in this chapter. (ISO/ASTM 52910 2018, p. 9.)

2.3.1 Support structures and build orientation

Support structures are generally required in L-PBF of metals. They are needed to anchor the part and conduct heat to the build platform during the build process. These structures are also required to prevent warping or build failures and to support any overhanging features. Parts and support structures need to be designed in a way, that the removal of supports is possible. (Diegel et al. 2019, p. 138; ISO/ASTM 52910 2018, p. 21, Wohlers et al. 2019, p. 214.)

The need for support structures can be affected by design choices to some extent. A general rule of thumb is that angles higher than 45° from horizontal do not require support. This,

however, is very material dependent and smaller angles will result in drastically worse surface quality (Klingaa et al. 2019, p. 1). The build orientation can be altered to minimize the need of support. (Das et al. 2015, p. 343; Diegel et al. 2019, p. 138; Wohlers et al. 2019, p. 214-215.) Example of this is presented in Figure 10.

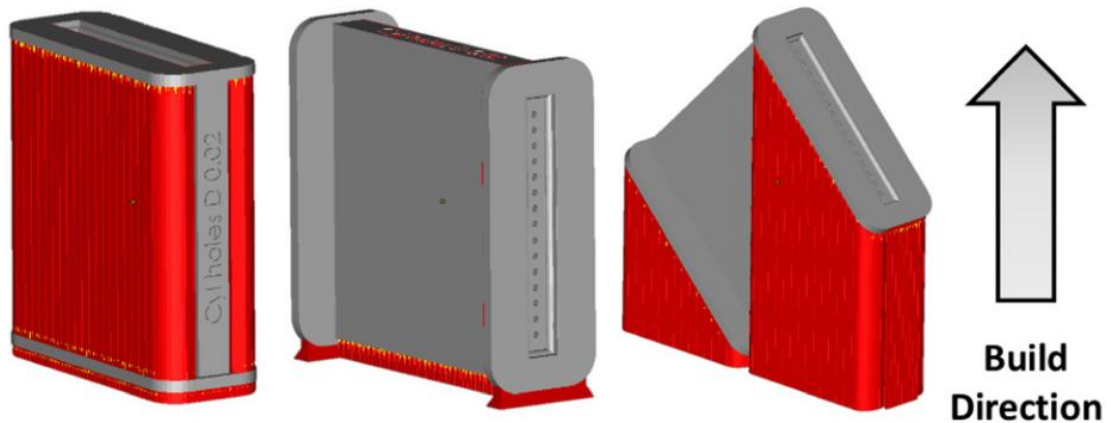


Figure 10. Effect of build orientation on the need of support structures (red) (Snyder et al. 2015, p. 2).

As can be observed from Figure 10, the amount of required support structures is dependent on the build orientation. As support structures need to be mechanically removed, they will directly affect the time it takes to post-process the part. (Diegel et al. 2019, p. 138–139; ISO/ASTM 52910 2018, p. 21, Wohlers et al. 2019, p. 214.)

Large horizontal surfaces will generally require stronger supports than is required elsewhere in the part. Melting wide areas of metal will result to substantial residual stresses once the metal solidifies and cools down. (Diegel et al. 2019. p. 139-140; ISO/ASTM 52910, 2018, p. 14.) An example of this is presented in Figure 11.

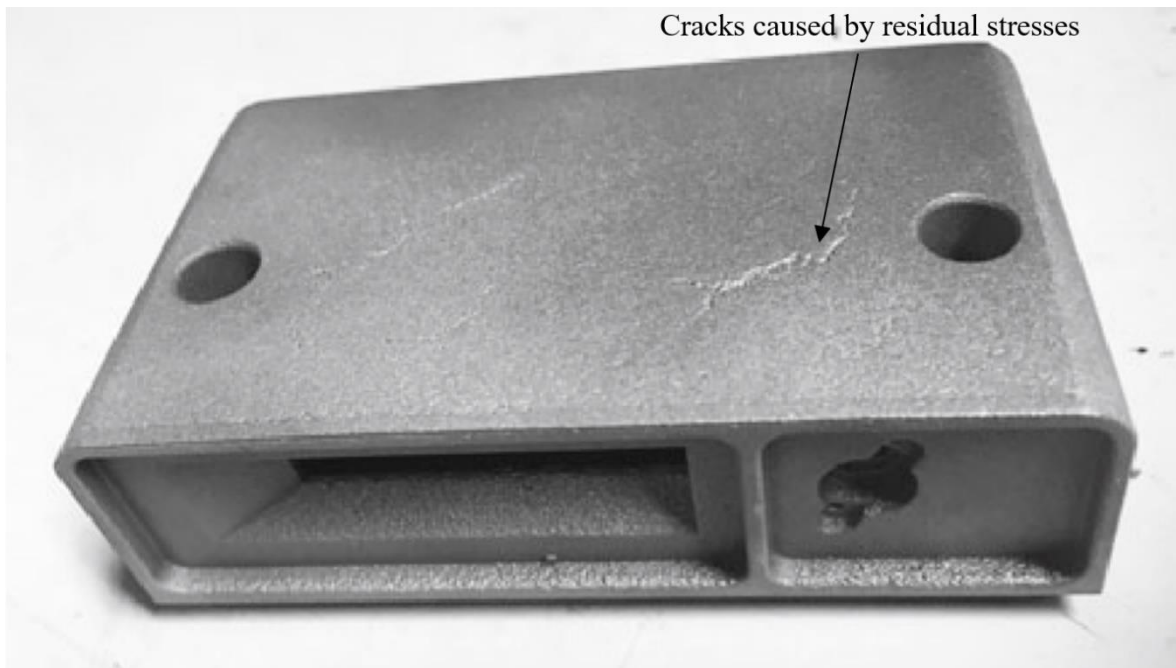


Figure 11. Large horizontal surface resulting to substantial residual stresses during the build process. Cracks caused by residual stresses highlighted. (Modified from Diegel et al. 2019, p. 140.)

As the seen Figure 11 presents, the large residual stresses can cause cracks, if the surface is not strongly supported. This can be asserted by choosing the build orientation, on which no large horizontal surfaces need to be melted. However, tall and thin structures should also be avoided, as they also are prone to brake during the building process. (Diegel et al 2019. p. 139–140; ISO/ASTM 52910 2018, p. 14.)

The build orientation affects build times. Usually, the higher the part is, the longer it takes to print. In some cases more parts can be fit on single building platform by printing them in vertical position. This affects the amount of parts that can be manufactured in one run. Therefore, the determination of build orientation is always a compromise between multiple aspects, such as manufacturing time and part quality. (Diegel et al. 2019, p. 139; Oh et al. 2018 pp. 131–132.)

2.3.2 Residual stresses

Melting wide horizontal surfaces will result in substantial residual stresses (Diegel et al. 2019. p. 139). Even while avoiding features like this, parts manufactured with L-PBF will

always have residual stresses because of the heat inherent to the process (Kruth et al. 2004, p. 617).

The formation of residual stresses is driven by two mechanisms on small scale: the temperature gradient mechanism (TGM) and the cool down mechanism (Simson et al. 2017, p. 185). The TGM is illustrated in Figure 12.

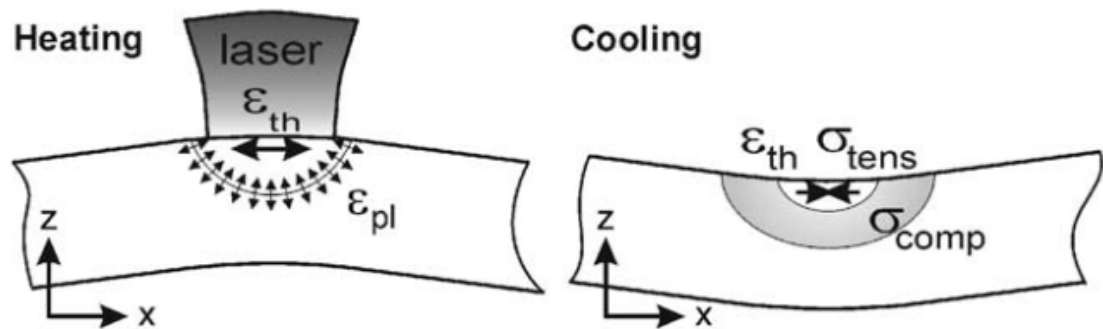


Figure 12. Formation of heat related residual stresses due to TGM. (Kruth et al. 2004, p. 618).

As the Figure 12 presents, the material expands due to heating and shrinks due to cooling. During the L-PBF process, laser melts the powder and strongly heats material causing it to expand (ϵ_{th} in Figure 12). This expansion is restricted by the surrounding material, causing compressive stresses (σ_{comp} in Figure 12). When the material yield stress, which is lowered due to heating, is exceeded, it is plastically compressed (ϵ_{pl} in Figure 12). Once the heating is stopped, thermally expanded material cools down and shrink, leading to bending towards laser beam and causing tensile stresses (σ_{tens} in Figure 12) to be generated in the formerly expanded area. (Kruth et al. 2004, p. 617; Simson et al. 2017, pp. 184–185.)

The cool down mechanism is caused by the temperature difference between successive layers (Simson et al. 2017, p. 185). This is presented in Figure 13. The cool down mechanism causing residual stresses. In L-PBF manufacturing process, residual stresses are formed due to the temperature differences of successive layers. (Modified from Simson et al. 2017, p. 185)

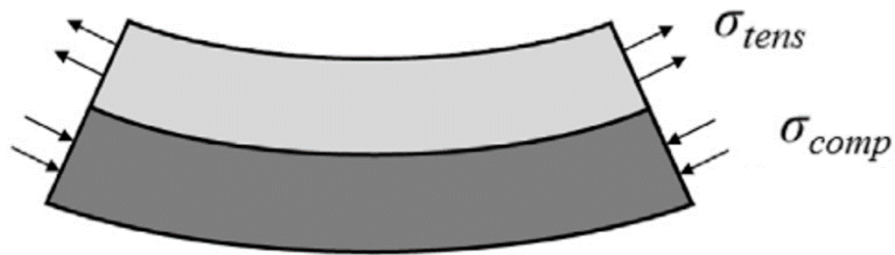


Figure 13. The cool down mechanism causing residual stresses. In L-PBF manufacturing process, residual stresses are formed due to the temperature differences of successive layers. (Modified from Simson et al. 2017, p. 185)

As can be seen from the Figure 13, tensile stresses are formed on the upper layer and compressive stresses on the underlying ones. This is because the two layers are metallurgically connected and the hot deposited layer contracts more than the colder layers below. (Simson et al. 2017, p. 185.)

The residual stresses should be considered in the design process as they can result to excessive deformations and cracks in parts. These deformations occurring during the build can interrupt the whole process. An example of this is presented in Figure 14. (Diegel et al. 2019, pp. 146–147.)

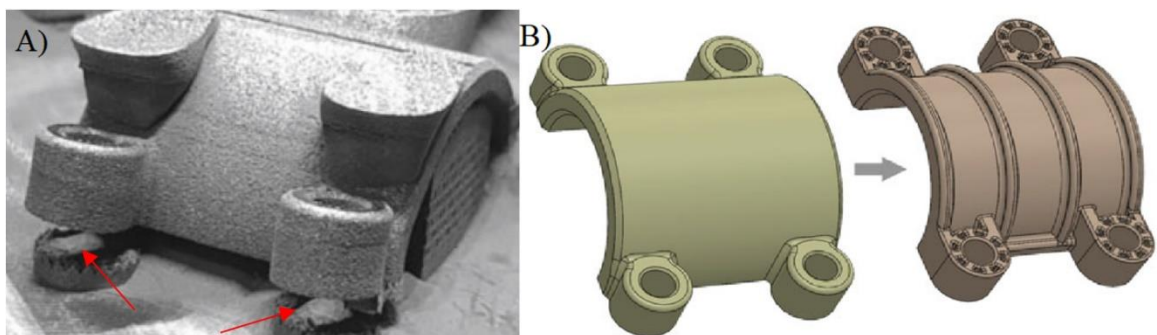


Figure 14. a) Part detached from build platform (red arrows) due to excessive residual stresses, b) redesign of the part for successful print. (Modified from Diegel et al. 2019, pp. 146–147.)

As Figure 14 shows, the magnitude of stresses can to some degree be affected by design choices. Following features should be avoided to minimize residual stresses:

- wide horizontal areas
- sudden changes in feature thickness
- sharp corners
- excess material.

The need for post process heat treatment and risk of build failure are minimized by avoiding these features. (Diegel et al. 2019, pp. 146–147; ISO/ASTM 52910 2018, p. 21; Wohlers et al. 2019, pp. 223–224.)

2.3.3 Material properties

The microstructure of L-PBF parts, which is the results of fast and directional cooling during the process, is different from their traditionally manufactured counterparts. In addition, the parts have some porosity and are not 100 % dense. The mechanical properties are dependent on these factors and differ from conventionally manufactured ones. In general, the strength of common additively manufactured alloys is comparable or higher than conventionally manufactured ones, while the ductility and fatigue strength are worse. (Brandt 2017, pp. 61–70; Yang et al. 2017, pp. 84–85.)

As the mechanical properties depend on the porosity and microstructure, the properties achieved with additive manufacturing are process dependent. The achieved porosity and microstructure vary based on used parameters. Process parameters, such as laser power and scanning speed, as well as material parameters, such as powder particle size distribution and flowability affect the final part properties. Parameters vary between L-PBF systems and should be considered in the design process. (Brandt 2017, pp. 68-69; Yang et al. 2017, p. 85.)

The fatigue properties of AM parts differ from conventional ones. Internal pores and defects, surface roughness, residual stresses and microstructure affect the fatigue life of metal parts. Pores and rough surface can act as stress concentrations accelerating the crack initiation. In addition, the crack propagation can be easier along the layer interfaces. These defects can be affected with post processing. However, it is important to consider that the design freedom of AM can be leveraged to minimize stress concentrations caused by part geometry and thus

considerably increase the fatigue life of the part. (Afkhami et al. 2019, p. 81; Diegel et al 2019, p. 149; Milewski 2017, p. 56; Yang et al. 2017, p. 118.)

The mechanical properties of AM parts are anisotropic meaning that they differ based on loading direction. Therefore, AM parts have different properties based on their build orientation. This is attributed to defect orientation and anisotropic microstructure. (Brandt 2017, pp. 68–69; ISO/ASTM 52910 2018, p. 16; Yang et al. 2017, pp. 117–118; Milewski 2017, p. 222.) This is presented in Figure 15.

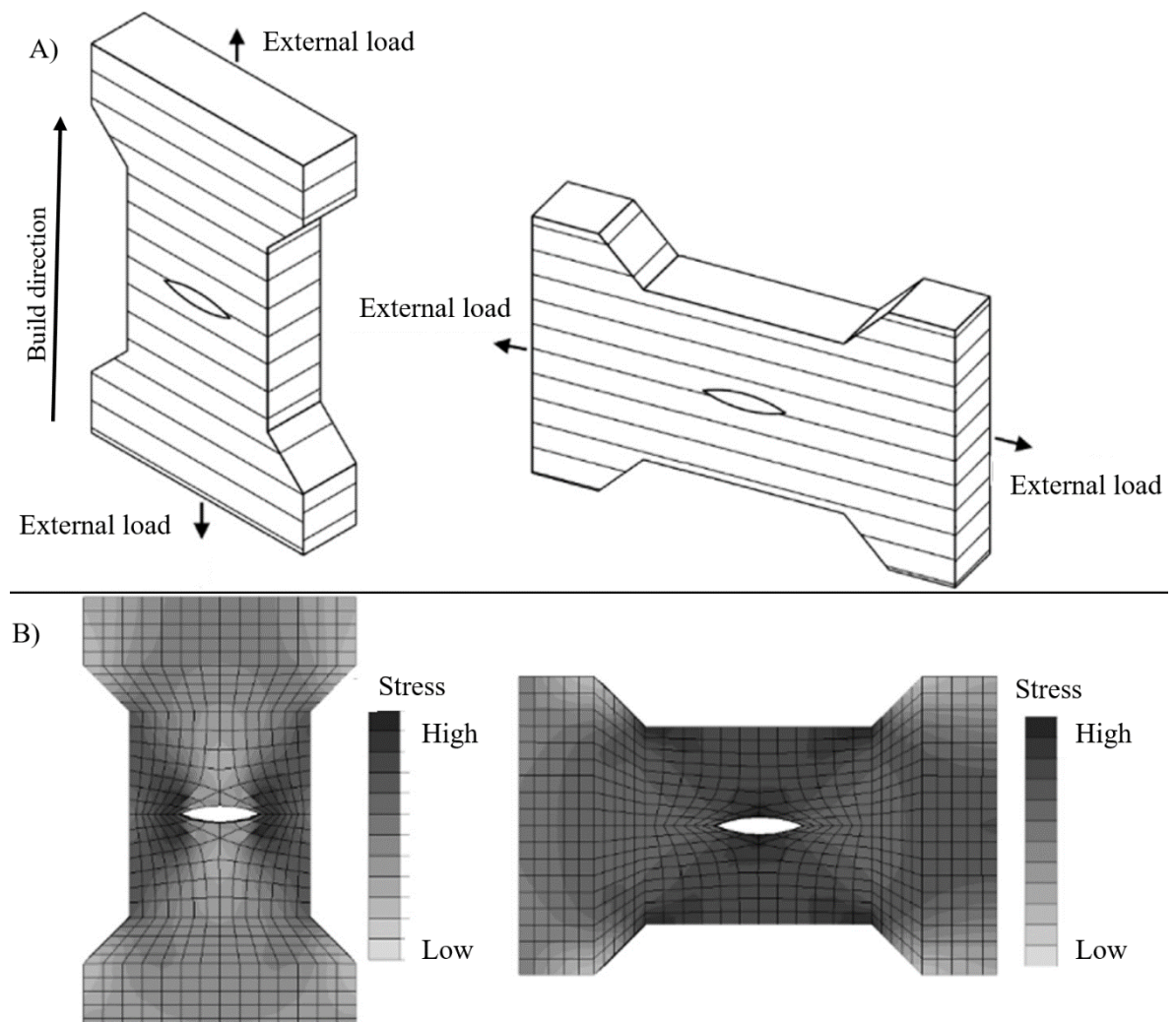


Figure 15. a) Build orientation and loading direction, b) Effect of defect orientation on loading direction. (Modified from Afkhami et al. 2018, p. 77).

As can be seen from Figure 15, layer and defect orientation change relative to loading direction based on build orientation. Generally, parts manufactured horizontally to the loading direction have higher strength properties than ones manufactured vertically, because of different layer orientation and microstructure. Fatigue strength is worse for vertically manufactured part because of the higher stress peaks caused by defects. The anisotropy can to some degree be affected with heat treatments and hot isostatic pressing (HIP), but still needs to be understood by the designer. (Brandt 2017, pp. 68–69; ISO/ASTM 52910 2018, p. 16; Yang et al. 2017, pp. 117–118; Milewski 2017, p. 222.)

2.3.4 Problems in DfAM

Most of the research and guidelines for DfAM focus mainly on the advantages of AM rather than its limitations. Some general design rules for AM have been developed, but they usually are very material, parameter and system dependent. For example, minimum wall thickness that can be manufactured varies between different L-PBF machines even with same materials. (Yang & Zhao 2015, p. 334.)

Some problems regarding material properties also linger. Properties, such as fatigue and creep strength of AM materials, are not yet fully understood and can affect the use of AM parts in some applications. The anisotropic and geometry dependent mechanical properties are also concern, as they can be difficult to consider during the optimization and design process. AM materials are currently missing systematic material property data and compiling such databases will take time. (Yang et al 2017, pp. 68–69; p. 126; Milewski 2017, p. 54.)

American National Standards Institute (ANSI) has recognized these design related problems. Additive Manufacturing Standardization Collaborative (AMSC) is an effort coordinated by ANSI, and in its roadmap, standardization of following design aspects is determined as a high priority:

- application specific design rules and guidelines
- dimensioning and tolerancing requirements.

While this activity is still ongoing, it highlights the need for standardization and further development in these areas. (Leach et al. 2019, p. 4)

3 BUILD PROCESS SIMULATION

L-PBF of metals is slow and expensive manufacturing process. This makes the build process simulation an important DfAM tool, as it can be leveraged to predict build and part failures. By utilizing FEA, the residual stresses and corresponding deformations developed during the build process can be evaluated. This allows the manufacturability of the design to be verified before manufacturing. Based on the result, part geometry can also be compensated to better match intended shape as printed. (Diegel et al. 2019, pp. 76–77; Milweski 2017, pp. 105–106.)

The build process simulations are computationally expensive. Simulations considering the complex real-life phenomena occurring during the build process can be very difficult to implement and have computational times exceeding the actual build time. Simulation of each individual laser pass on powder bed requires fine FE mesh and small time increments. Therefore, most of the research on L-PBF process simulations focus on geometries with very limited size, as simulations with this method have run times of hundreds of hours for even modestly sized geometries. (Bugatti & Semeraro 2018, pp. 330–331; Diegel et al. 2019, pp. 76–77; Gouge et al. 2019, pp. 1–2, Milewski 2017, pp. 105–106.)

Because of the problems inherent to the direct modeling of individual laser passes, modeling approaches have been proposed to allow the simulation of industrial size parts in reasonable time. Two general methods for this have been used:

- thermo-mechanical methods
- inherent strain methods.

Different variations within these methods have been proposed, with all of them approximating the process to simplify the analysis considerably. Simplifications are necessary to decrease the computational times, while they also introduce some potential limitations. (Bugatti et al. 2018, p. 330; Gouge et al. 2019, p. 2.) Examples of thermo-mechanical method variations and inherent strain method are presented in more detail in this chapter.

In L-PBF simulations, the material deposition inherent to AM needs to be modeled. The simulation of this in FEA is traditionally achieved through element birth or quiet element methods. The element birth technique adds a new set of elements during each time increment through model change. The quiet element method assigns negligible material properties to all elements, until they are activated to simulate the material deposition. (Gouge & Michaleris 2018, p. 10; Yang et al. 2019, p. 7.)

3.1 Inherent strain approach

The inherent strain approach works by first determining the plastic strain developing during manufacturing process and then applying it to the part scale model. Flow chart for inherent strain method is presented in Figure 16.

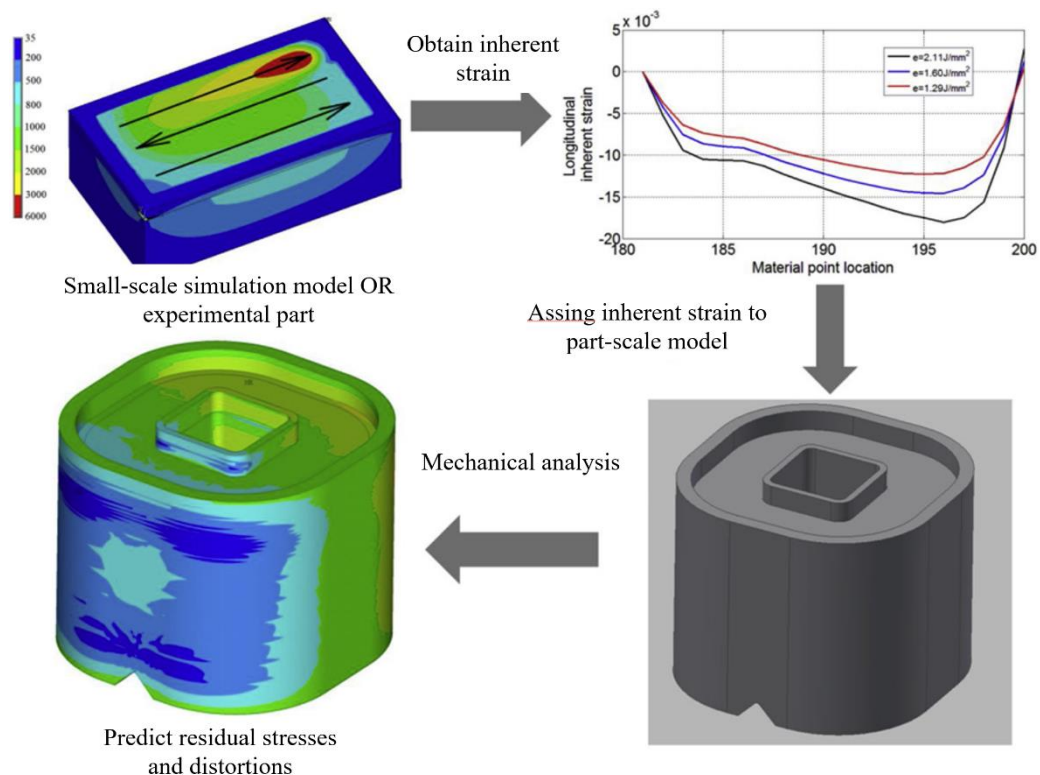


Figure 16. Flow chart for inherent strain method (Modified from Chen et al. 2019, p. 408).

As the Figure 16 presents, the determination of plastic strain can be done by measuring strains from small physically built components. The inherent strain method with manual measurements is the most commonly used simulation method in commercial software (Gouge et al. 2019, p. 2). Another option to determine the plastic strains is to calculate them

from a small-scale thermo-mechanical simulation model. (Chen et al. 2019, p. 407; Gouge et al. 2019, p. 2; Bugatti & Semeraro, 2018, p. 331).

The inherent strain method, where strains are measured from small-scale simulation model, is presented by Chen et al. (2019, pp. 406–418). Method was used to predict distortions and residual stresses of cantilever beam and canonical square structure manufactured via L-PBF. The results were then compared to corresponding values measured from physically built components and to values predicted by commercial simulation software Simufact Additive. This software is based on the inherent strain method, where strain values are measured from experimental part. (Chen et al. 2019, p. 406; p. 413) The distortion profiles comparing results from simulation and measured values for both geometries are presented in Figure 17.

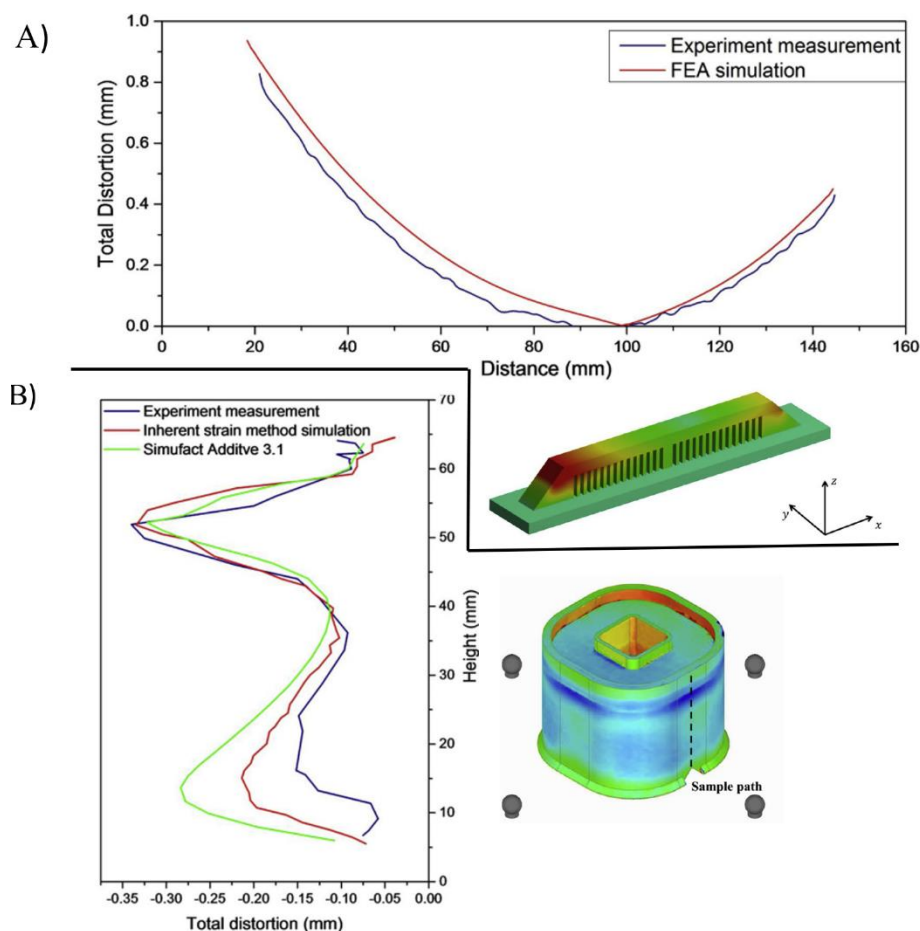


Figure 17. Distortion profiles of simulated and physically built parts. a) Cantilever part, distortion measured from center line of the top surface of the part, b) canonical square structure, distortion measured along straight line from vertical edge. Geometries and displacement contours also presented. (Modified from Chen et al. 2019, pp. 415–416.)

As it can be observed from Figure 17, the results agree closely with experimental results. Distortion trend is similar for the cantilever part (Figure 17a), with magnitude being overestimated by a maximum of 11 %. Trend is also similar for canonical square structure (Figure 17b). Distortion predictions match very closely at the top of the part, difference only being 1 %. However, the method overestimated the distortion by 35 % near bottom of the part. The software based on experimentally measured strain values overestimated the distortion even more. (Chen et al. 2019, pp. 414-416.)

Advantage of the inherent strain method is that it does not require input of temperature dependent material properties. It also requires only a relatively short computational times because only mechanical simulation is required to predict stresses and deformation. However, as the strain values are obtained only from a small scale, uniformity of strains formed throughout the build process is assumed. Therefore, geometrical effects on thermal history and distortions are not considered. This can lead to loss of accuracy and unexpected behavior of the model in some geometries (Bugatti & Semeraro 2018, pp. 329–332; Gouge et al. 2019, p. 2.)

3.2 Thermo-mechanical methods

In the thermo-mechanical method, the temperature distribution is obtained from thermal analysis and is then imported into the mechanical analysis as thermal load to generate stresses and strains. Thermal and mechanical analyses are typically weakly coupled, meaning that the mechanical behavior is affected by the thermal history but not vice versa. Weakly coupled analysis is preferred over fully coupled, as it considerably decreases the computational time and is a fair approximation for AM processes. (Denlinger & Michaleris 2016, p. 52; Gouge & Michalaris 2018, p. 20; Yang et al. 2019, p.p 2-4; Zhang et al. 2004, p. 624.)

The thermal analysis is governed by following equation for transient heat conduction:

$$Q + \nabla \cdot (k\nabla T) = \rho C \frac{\partial T}{\partial t} \quad (1)$$

where Q is the internal heat generation, k is the thermal conductivity, T is the temperature, t is the time, ρ is the density of material, and C is the specific heat capacity. (Gouge et al. 2019, p. 4; Panda & Sahoo 2019, p. 1374; Williams et al. 2018, p. 417.)

The heat loss is taken into account by considering heat transfer due to convection and radiation, which can be calculated by equations for Newton's law of cooling and Stefan-Boltzmann law respectively:

$$q_{conv} = h(T - T_0) \quad (2)$$

$$q_{rad} = \sigma\varepsilon(T^4 - T_0^4) \quad (3)$$

where q_{conv} is the heat transfer due to convection, h is the heat transfer coefficient, T_0 is the ambient temperature, σ is the Stefan-Boltzmann constant and ε is the emissivity. (Gouge et al. 2019, p. 4; Panda & Sahoo 2019, p. 1374; Yang et al. 2019, p. 7.)

The results of the thermal analysis are used to evaluate the residual stress and distortion according to governing stress equilibrium equation:

$$\nabla \cdot \sigma = 0 \quad (4)$$

where σ is the stress, calculated with following equation for the mechanical constitutive law:

$$\sigma = C(\varepsilon_e + \varepsilon_{pl} + \varepsilon_{th}) \quad (5)$$

where C is the material stiffness tensor and ε_e , ε_{pl} and ε_{th} are the elastic, plastic and thermal strain components respectively. The thermal strain component driving the residual stress is calculated according to following equation:

$$\varepsilon_{th} = \alpha \cdot \Delta T \quad (6)$$

where α is the thermal expansion coefficient and ΔT is the change in temperature. (Gouge et al. 2019, p. 4; Panda & Sahoo 2019, p. 1374; Williams et al. 2018, p. 417.)

Thermo-mechanical analyses require input of temperature-dependent data of material properties. Because of the large temperature differences during the manufacturing process, the material experiences wide range of temperatures and physical states. Material properties can vary greatly between different states and thus should be input as temperature dependent for the analysis. (Yang et al. 2019, p. 5; Gouge & Michaleris 2018, pp. 12–14.) However, engineering judgement along with experiments should be used to determine properties which require temperature dependence. Inputting properties which are negligibly affected by heat as temperature dependent will needlessly increase non-linearity and computational times (Gouge & Michaleris 2018, p. 12.)

In thermo-mechanical methods, the heating of individual laser scans is usually approximated by activating full layer groups at elevated temperatures. During each time increment, element groups presenting some number of layers are activated at a temperature calculated based on the real build parameters to calculate the thermal history of the part. This thermal history is then imported on part scale mechanical simulation to calculate the mechanical response. (Gouge et al. 2019, p. 2; Williams et al. 2018, p. 417; Yang et al. 2019, p. 2.)

A variation of thermo-mechanical approach has been presented by Yang et al. (2019, pp. 1–11). A software based on Abaqus 2018 FE solver was used to simulate the build process of a one of four cantilever parts made from Inconel 625 on single build platform and results were compared to physically built part. (Yang et al. 2019, p. 1.) The geometry of the part and their orientation on physical build platform is presented in Figure 18.

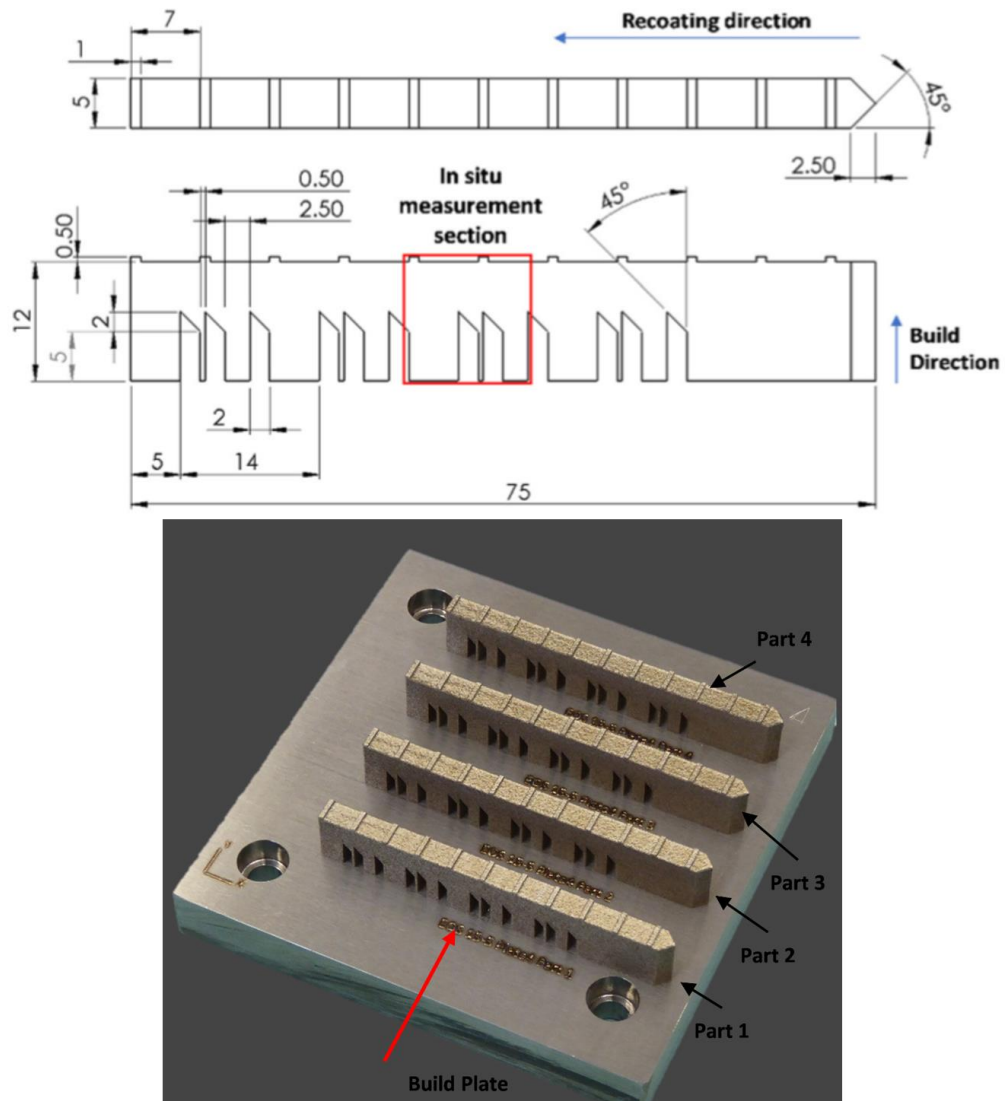


Figure 18. Geometry of the part used for build process simulation. Build process of one (marked with red arrow) cantilever part was simulated. (Modified from NIST 2018.)

As can be seen from Figure 18, the physical build platform includes four cantilever. Simulation model was simplified to only include the part under interest instead of modeling the whole build plate with four parts to reduce computational time. Simplification was deemed justifiable, as spacing between each part is enough for the build of adjacent parts to have negligible effect on thermal history of other parts. Therefore, a single cantilever part on scaled down build platform was modeled. The build platform size used was deemed to be sufficient to accurately present the heat sink effect of real build platform. (Yang et al. 2019, pp. 4-5.) The FE model is presented in Figure 19.

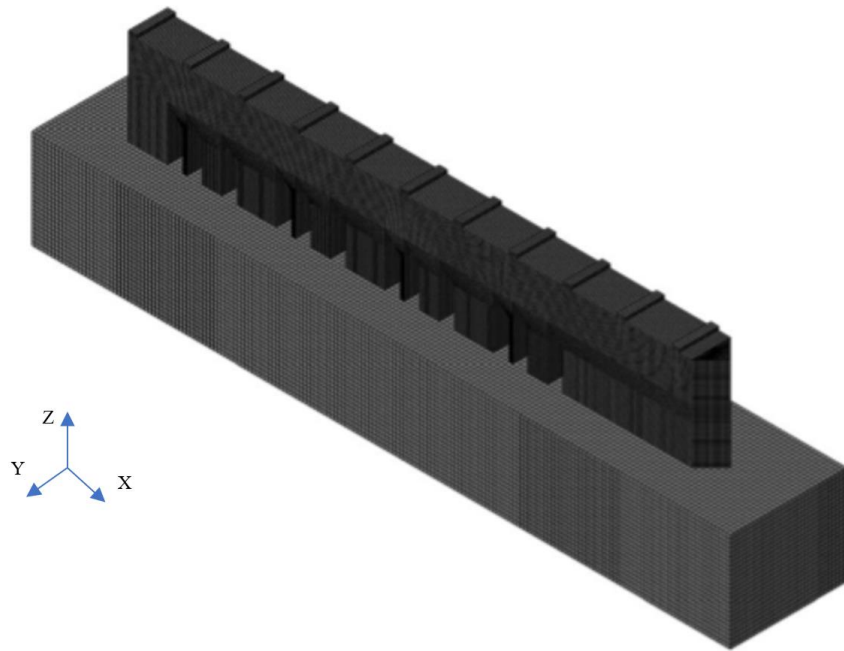


Figure 19. FE model of the cantilever part on build platform. (Yang et al., 2019, p. 5.)

As the Figure 19 depicts, linear eight node hexahedron elements were used for the FE mesh of the model. The real layer thickness used in the build was 0.02 mm. Using corresponding element size would be unfeasible due to large number of layers. Element size of 0.2 mm was used, meaning each element layer represents approximately 10 real layers. This was deemed to be justifiable compromise between accuracy and computational time. Fixed boundary condition was set on bottom of the build platform mesh and meshes of cantilever part and built platform were connected. (Yang et al. 2019, pp. 4–5; p. 9.)

Material properties for Inconel 625 were extracted from literature. Density, latent heat and solidus and liquidus temperatures were input as temperature independent. Thermal conductivity, specific heat capacity, Young's modulus, Poisson's ratio and thermal expansion coefficient were input as temperature dependent. In addition, plasticity was input based on one stress-strain curve only, rather than inputting curves for multiple temperatures. This was justified by citing other studies applying similar method, where temperature dependent behavior for plasticity was deemed not important. (Yang et al. 2019, pp. 5–6.)

Laser beam was modeled as concentrated point heat source, where heat flux is applied at a singular moving point and the heat then dissipates through the model, as presented in

equation 1 for heat conduction. The movement of the laser beam was modeled to replicate the real movement of the laser beam. The toolpath-mesh intersection module available within Abaqus was leveraged to identify all elements which the laser passes through at each time increment. This allowed the heat source to be properly distributed within each time increment. Heat loss within the model was taken into account through convection and radiation, as presented in equations 2 and 3 respectively. The effect of powder bed surrounding the part present in real build was not considered for convection, as its effect was deemed minimal by conducting number of sensitivity studies. (Yang et al. 2019, pp. 4–7.)

The material deposition within the model was modeled by applying the element birth method. Furthermore, progressive element activation feature within Abaqus, which allows the partial activation of elements, was used to accurately model the real deposition of material. (Yang et al. 2019, pp. 4–7.)

After the thermal analysis was completed, the thermal history was imported into the mechanical model. Thermal expansions, used to calculate residual stresses, were then calculated based on this thermal history. Initial temperature for activated elements within the mechanical model was set to match the relaxation temperature of the Inconel 625. This is the temperature above which thermal stresses experienced by the material are negligible. (Yang et al. 2019, pp. 8–9.)

From the results of the simulation, residual strains in the x and z direction (see Figure 19) were plotted (Yang et al. 2019, pp. 8–9). These contour plots are presented in Figure 20.

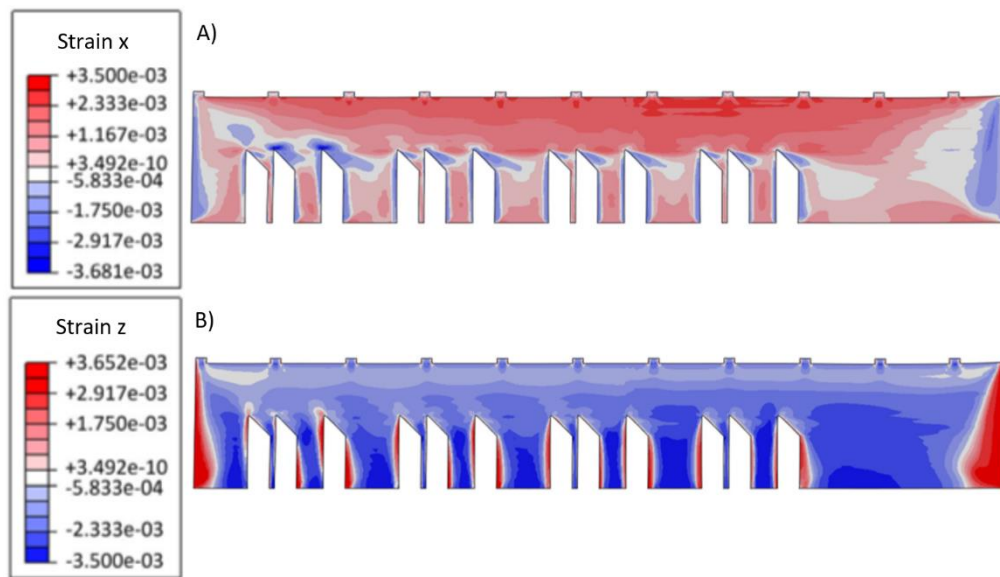


Figure 20. The predicted residual strain contour plots in the a) x and b) z directions. (modified from Yang et al. 2019, p. 8).

As it can be observed from Figure 20, the strain x values vary from -0.0037 to 0.0035, with the main body showing tensile strains and edges compressive strains. Strain z contour plot is almost a mirror image of this, with values ranging from -0.0035 to 0.00368. (Yang et al. 2019, p. 10.) The corresponding strain contour plots measured with X-ray diffraction (XRD) from built part are presented in Figure 21 (Yang et al. 2019, p. 8).

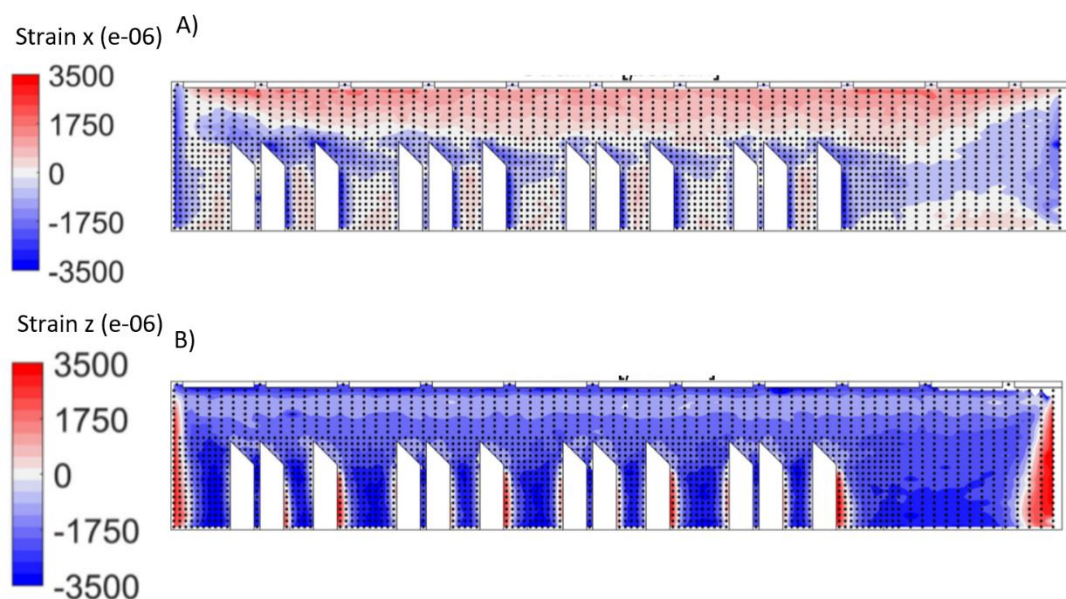


Figure 21. XRD measured residual strain contour plots in the a) x and b) z directions. (Yang et al. 2019, p. 8).

As it can be seen from Figure 21, the XRD measured strains vary from between $\pm 0,0035$. This is in close agreement with the values predicted by simulation model, with peak values differing only marginally for both strain directions. The strain contour plots also agree very closely. (Yang et al. 2019, p. 8)

Unlike inherent strain method, thermo-mechanical models on part scale take into account the geometric effects on the thermal history. This method, however, does not consider the plasticity induced by the laser beam, as individual laser scans are not included in the model while activating complete layers at elevated temperatures during time increment. This can lead to loss of accuracy in some cases. (Gouge et al. 2019, p. 2).

Variation of thermo-mechanical methods based on multi-scale simulation, effectively combining inherent strain and macro scale thermo-mechanical methods, is presented by Gouge et al. (2019, pp. 1–17). In this approach, thermo-mechanical analysis is done on two different scales to predict the residual stresses and distortions (Gouge et al. 2019, p. 5). The flowchart for this method is presented in Figure 22.

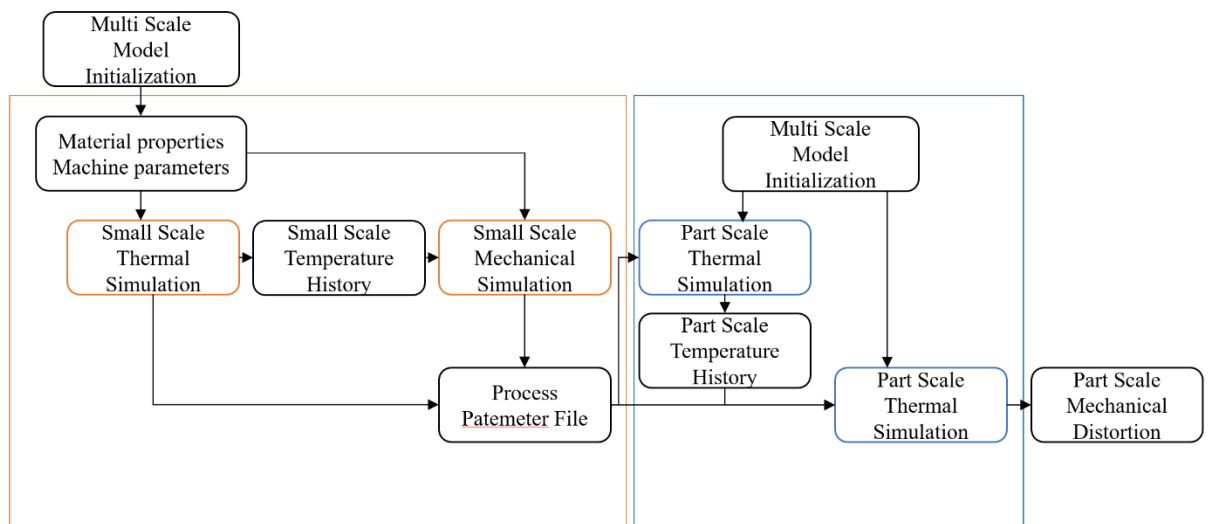


Figure 22. Flowchart for multi-scale simulation approach (modified from Gouge et al. 2019, p. 6).

As the Figure 22 shows, simulation is first done on small scale. At this scale, accurate analysis is conducted to capture interactions between layers. The results from this analysis are extracted and used in the part-scale analysis. (Gouge et al. 2019, pp. 5–6.)

The method was used to simulate the build process of three different components, applying a software using Pan Solver 2019.0. Results were compared to their physically built counterparts. (Gouge et al. 2019, p. 5) The geometries are presented in Figure 23.

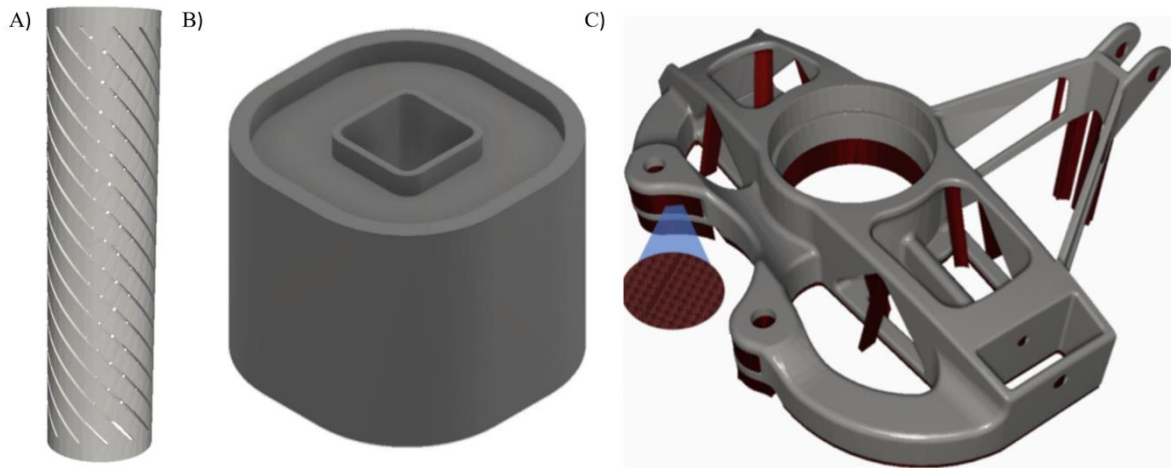


Figure 23. Geometries of the parts used in multi-scale simulation: a) Compliant cylinder, b) square canonical and c) Automotive upright (Modified from Gouge et al. 2019, pp. 3–4).

As it can be seen from Figure 23, parts have different geometries. The parts were built and simulated from different materials: a) from Inconel 625, b) from Inconel 718, and c) from AlSi10Mg. Simulation of the build process of various geometries and materials was done to test the capabilities of the simulation method across variety of conditions. (Gouge et al. 2019, p. 3; p. 10.)

Small and part scale models were FE meshed similarly. Both meshes consisted of 8-node hexahedral voxel elements. Elements were introduced into the models by applying element birth method (Gouge et al. 2019, p. 5; Neiva et al. 2019, p. 1102). In addition, adaptive meshing, available in Pan Solver 2019.0, was used. Adaptivity allows the FE mesh to change during the build process. Mesh is kept dense at the layer currently being deposited, while allowing elements to combine and coarsen the mesh as the build process moves further away from them, reducing the simulation time. (Gouge et al. 2019, pp. 5–7; Neiva et al. 2019, pp. 1101–1102; p. 1122.) For micro-scale model, the element size used at the currently simulated layer was set to match the melt pool size and layer thickness. In part-scale model, multiple layers were combined to one, resulting in larger element size. (Gouge et al. 2019, pp. 5–8.)

Temperature dependent material properties and process parameters corresponding real conditions were input for small scale simulation model. The process parameters included laser power, scan speed, laser absorptivity, bead radius, hatch spacing, layer thickness, scan pattern rotation between layer, and the recoating time. The heat source was modeled using the Goldak model. The heat conduction and loss were modeled according to equations 1, 2 and 3. The simulation was done as a weakly coupled thermo-mechanical analysis, to model a build of a block of ten 5 mm² layers. (Gouge et al. 2019, p. 5; p. 10)

The results of this analysis were imported into the part-scale model, alongside with temperature independent material properties. Fixed boundary condition was set at the bottom of the build plate. The analysis was done as weakly coupled thermo-mechanical analysis. The heat input was modeled by activating element layers at temperatures determined by the process parameters and part-scale thermal history was obtained. The mechanical analysis then maps the mechanical response information from the small scale results on the part-scale model. Simultaneously, the part scale mechanical response is calculated based on the part-scale thermal history. (Gouge et al. 2019, p. 5; pp. 10–11.)

Once the simulation was completed, displacement values were obtained from simulation models. Corresponding values were also measured from physically built parts. (Gouge et al. 2019, pp. 12–13.) The contour plots of displacement values for all physically built and simulated parts are presented in Figure 24.

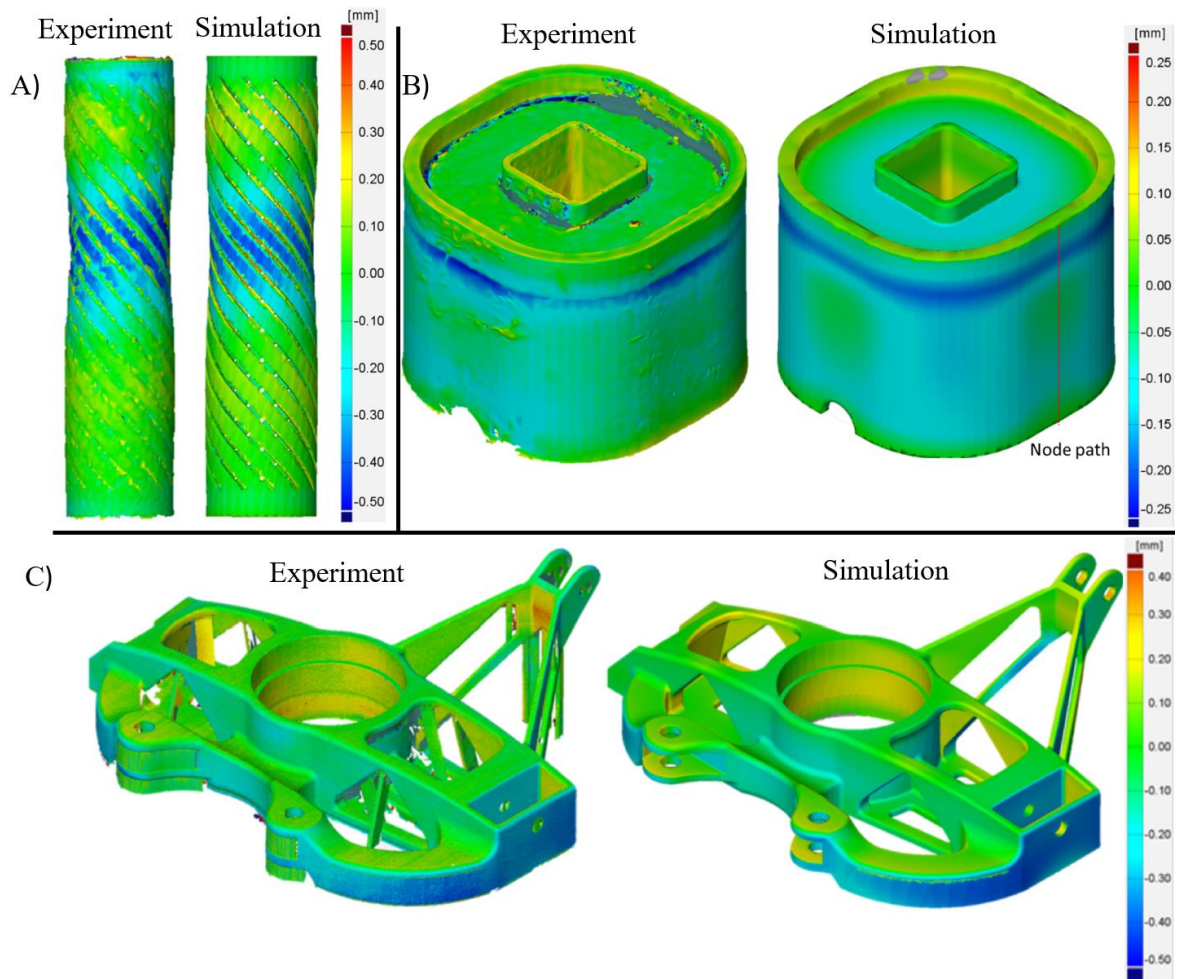


Figure 24. Displacement contour plots for physically built (Experiment) and simulated parts. (Modified from Gouge et al. 2019, pp. 12-15).

As can be observed from Figure 24, the displacement contours look similar for simulated and built parts. Results of obtained with multi-scale approach agree well with measured values, with the peak displacement values of each model showing maximum error of 13 %. In addition, the correlation between measured and simulated displacement values were at least 90.5 %. The method allowed relatively accurate results to be obtained for large components in about 10 % of the actual build time. (Gouge et al. 2019, p. 16)

4 CASE STUDY: ADDITIVELY MANUFACTURED ELECTRODE

The thesis was done as a part of ReGoldAM project funded by Academy of Finland. The project is done in co-operation with research group of Hydrometallurgy for Urban Mining. Goal of the project is to increase the efficiency of gold recovery from electronic waste streams through the use of electrochemical processes and additive manufacturing. During the project, novel electrochemical reactors are constructed by leveraging possibilities offered by AM. The project lasts from 01.09.2019 to 31.08.2023.

Aim of the case study was to design additively manufactured electrodes, which are used to enhance electrochemical gold recovery process. This process is subject of interest due to the increase of electronic waste and its high concentrations of gold (Kim et al. 2011, p. 206). The background for the used electrochemical process and electrodes is presented in this chapter.

4.1 Application of the electrochemical process

Electrochemical processes utilizing electrodes for the recovery of precious metals from electronic waste have generated interest due to the economic growth and technological advances resulting in the increase of this waste. One of the recovery methods is based on electro-generated chlorine (Cl_2), which is used to leach precious metals. This process has been proven to be advantageous, while also being environment friendly. (Kim et al. 2011, p. 206.)

The process has been demonstrated by Kim et al. (2011, pp. 206–211) for gold recovery purposes. The schematic figure of the process is presented in Figure 25.

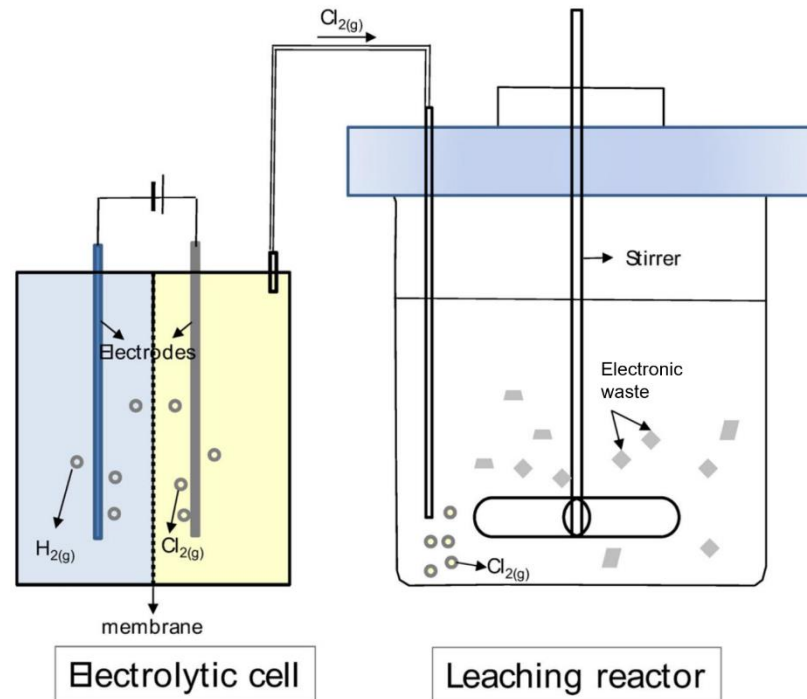


Figure 25. Gold recovery process from electronic waste. (Modified from Kim et al. 2011, p. 208)

As can be seen from Figure 25, the process requires two electrodes, cathode and anode, which are separated by membrane and submerged in hydrochloric acid solution. By supplying constant current, chlorine is generated on anode side. This electro-generated chlorine makes the gold dissolve from the electronic waste, making it possible to be recovered. (Kim et al. 2011, p. 207–209.) The assumption of the case is that the generation of chlorine could be enhanced by using a flow reactor and designing optimized electrodes manufactured with L-PBF. Example of flow reactor is presented in Figure 26.

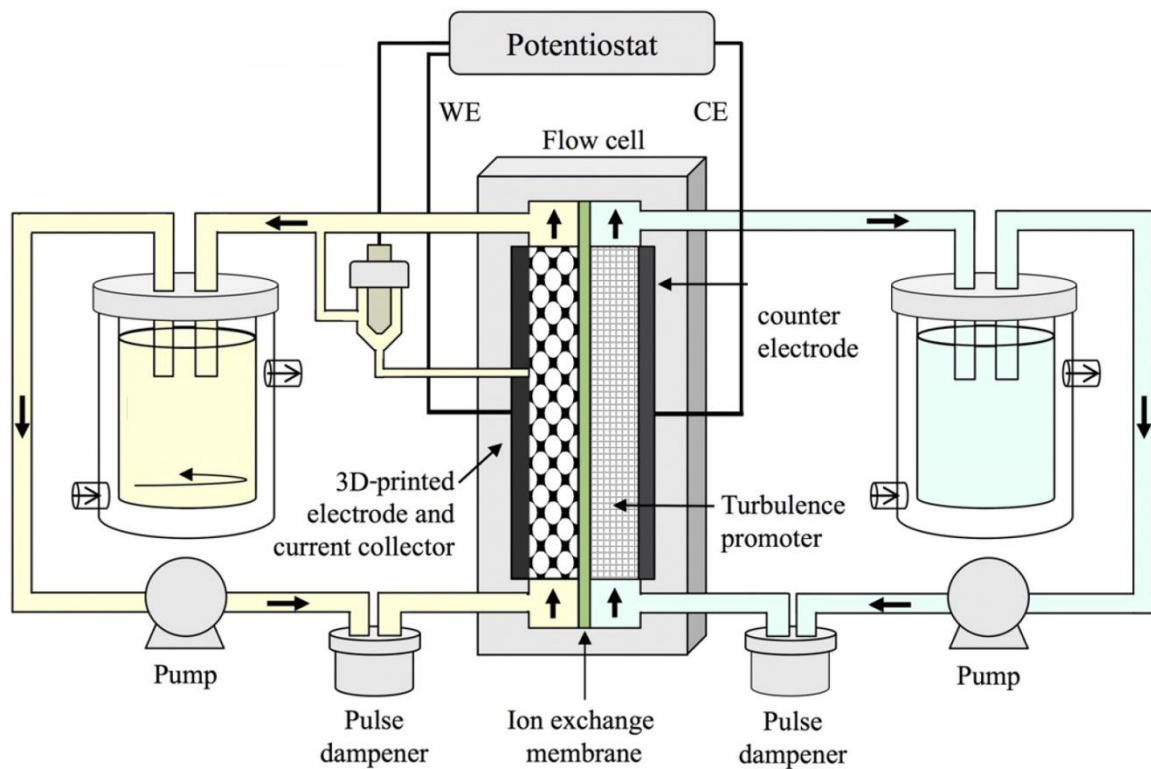


Figure 26. Example of flow reactor utilizing additively manufactured electrode (Modified from Arenas et al. 2017, p. 134).

As it can be seen from Figure 26, additively manufactured electrodes can be utilized in flow reactor. Porous electrodes, such as ones traditionally made from expanded metals, enhance the release of gaseous products (Pletcher & Walsh 1990, pp. 92–23). The features of the porous structure could be further optimized by utilizing AM (Arenas et al. 2017, p. 134).

4.2 Additively manufactured electrodes

Additively manufactured electrodes have shown promise by increasing performance of electrochemical processes. The freeform and porous features manufacturable with L-PBF offer advantages over traditional planar electrodes, as properties such as high surface area and enhanced flow profile can significantly increase the capabilities of the electrode. (Arenas et al. 2017, p. 133.) Additionally, electrodes manufactured via AM offer advantages over traditionally used three-dimensional electrodes, such as metal foams, because of structural uniformity, leading to higher electrical conductivity and surface utilization (Huang et al. 2017, p. 18176–18178).

The effectiveness of additively manufactured electrodes has been demonstrated by Arenas et al. (2017, pp. 133–137). In the study, electrode was manufactured via L-PBF from stainless steel. (Arenas et al. 2017, p. 133-134.) The electrode is presented in Figure 27.

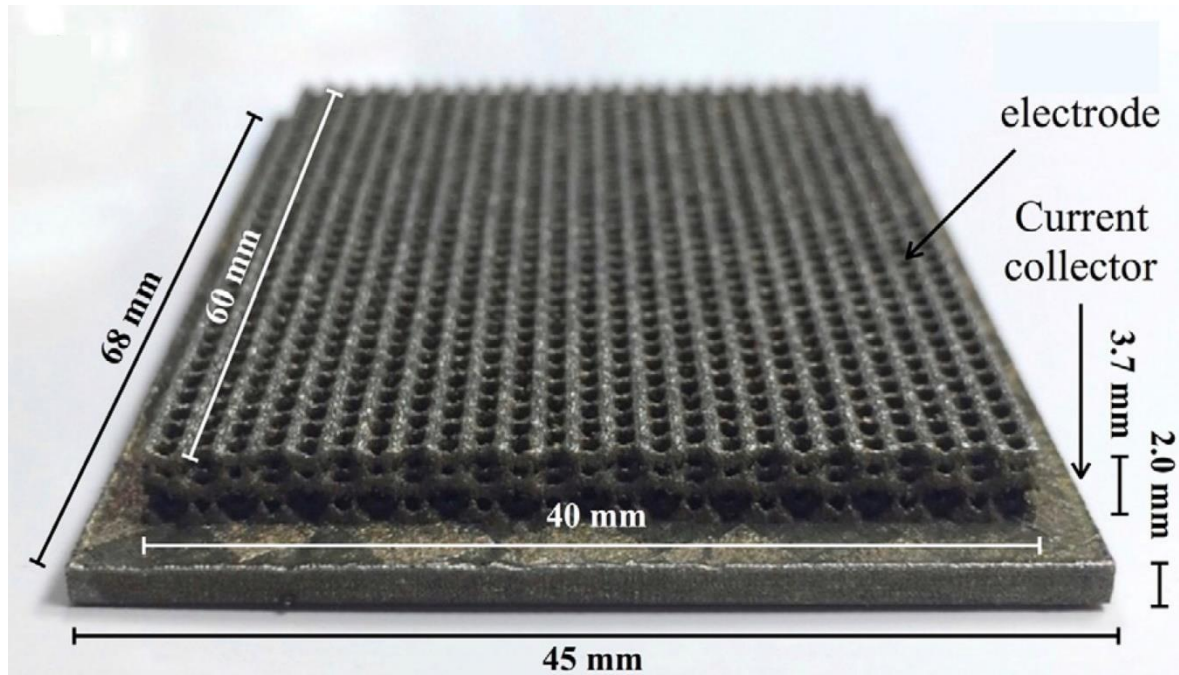


Figure 27. Stainless steel electrode manufactured via L-PBF (Modified from Arenas et al. 2017, p. 135).

As can be seen from Figure 27, the electrode is designed by utilizing lattices. The increased surface area achieved with this porous structure enhanced the electrode performance compared to common planar electrodes. Furthermore, the uniformity of porous and solid sections of the electrode and the high surface roughness achieved with additive manufacturing, were also deemed advantageous in this application. (Arenas et al. 2017, pp. 135–136.)

Catalytic 316L stainless-steel electrode for oxygen evolution reaction was manufactured via L-PBF and studied by Huang et al. (2017, pp. 18176–18182). In the study, electrode was designed by utilizing lattice structures, to obtain large surface area and uniform structure. These factors contributed to the increase electronic conductivity and efficient ion transport pathways, as well as decreased tendency to trap gas bubbles, leading additively manufactured electrode to demonstrate more uniform current distribution and larger

electroactive surface area over traditional metal foam electrodes. In addition, it showed better mechanical properties and corrosion resistance. (Huang et al. 2017, pp. 18176–18182.)

Electrodes manufactured via L-PBF have also been studied by Sun et al. (2019, pp. 11–17). In the study, porous three-dimensional electrode was manufactured from titanium powder and used for electropolymerization of nanofiber polypyrrole. (Sun et al. 2019, p. 11.) The electrode dimensions and structure are presented in Figure 28.

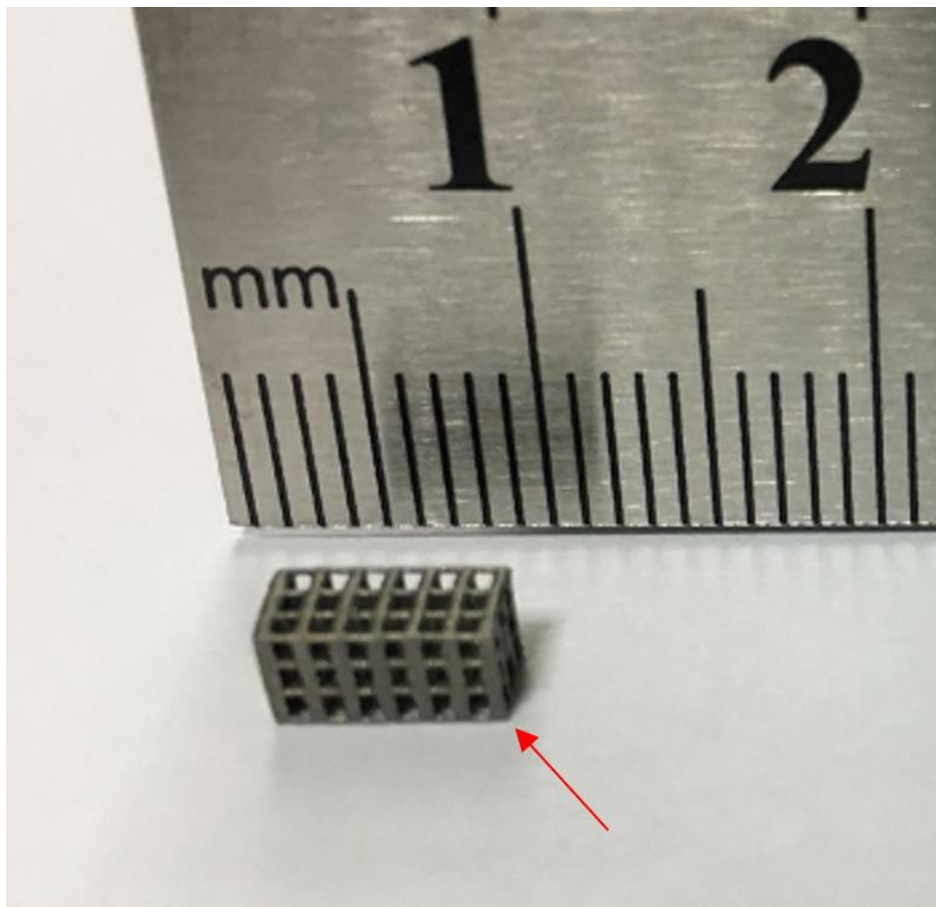


Figure 28. Titanium electrode (pointed with red arrow) manufactured via L-PBF (Modified from Sun et al. 2019, p. 12).

As can be seen from the Figure 28, the very simple lattice-like structure was used for the electrode design. In experiments, additively manufactured electrode performed worse than its planar counterpart, as the quality of polypyrrole nanofibers produced on inner surfaces were inferior to the ones produced on the outer surfaces. This was attributed to the non-uniform current distribution within the three-dimensional electrode, causing the

electropolymerization reaction to vary over the depth of the electrode. Regardless, potential to increase electrochemical activity due to increased surface area was recognized. (Sun et al. 2019, p. 11–17.)

4.3 Factors affecting electrode performance

Several different electrode-related aspects affect the electrochemical process. Electrode variables affecting the process are material, surface area, geometry, and surface condition. (Bard & Faulkner 2001, p. 20.)

4.3.1 Geometrical factors

The effectiveness of electrochemical processes highly depends on the surface area of the electrode, as the reaction rate of the process at fixed current density is directly proportional to the electroactive area. Therefore, maximizing the surface area of the electrode while minimizing its occupied volume will increase the efficiency of the reactor. This is demonstrated by the volumetric mass transport coefficient, which is a useful figure to assess the reactor performance (Pletcher & Walsh 1990, p. 82):

$$k_m A_e = \frac{k_m A}{V_e} \quad (7)$$

Where $k_m A_e$ is the volumetric mass transport coefficient, k_m is the mass transport coefficient, A_e is the electroactive area of the electrode per unit volume, A is the electroactive area and V_e is the electrode volume. (Pletcher & Walsh 1990, pp. 79–83.) In addition, the value for k_m depends on the electrode geometry, orientation, volumetric porosity and surface roughness, which can be controlled through design when electrode is additively manufactured (Arenas et al. 2017, p. 134).

Fractional conversion, which is the ratio of reactant amount reacted to the reactant amount fed, of the reactor can be described by following equation (Pletcher & Walsh 1991, p. 62):

$$X_A = 1 - \exp - \frac{k_m A_e L}{v} \quad (8)$$

Where X_A is the fractional conversion, L is the electrode length and v is the mean linear velocity of the flow. In addition, k_m is as follows (Pletcher & Walsh 1991, p. 62):

$$k_m = \alpha v^\beta \quad (9)$$

Where α and β are empirical constants and increasing with the flow turbulence. When this is substituted into equation 8, following equation is achieved (Pletcher & Walsh 1991, p. 62):

$$X_A = 1 - \exp(-\alpha A_e L v^{\beta-1}) \quad (10)$$

The equation 10 shows that the electrode length and electroactive surface area are the most important factors affecting the fractional conversion of the reactor, with flow velocity and turbulence also affecting. (Pletcher & Walsh 1991, p. 62) The same is presented in Figure 29.

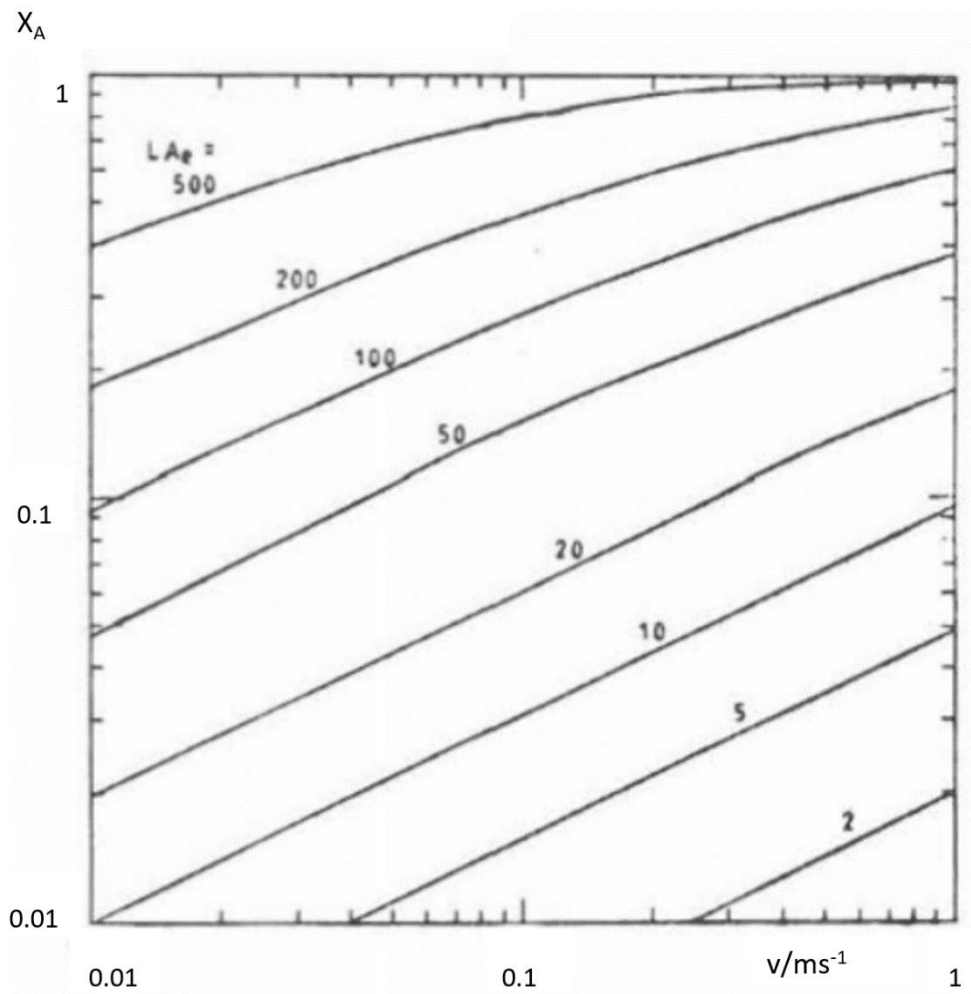


Figure 29. Fractional conversion as a function of mean linear flow velocity for a single pass in flow reactor. Behavior is idealized to demonstrate importance of electrode length and electroactive area. α and β are assumed to be 0.01 and 0.5, respectively. (Pletcher & Walsh 1991, p. 64.)

As the Figure 29 depicts, the effect of electrode length and electroactive surface area are the most important factors affecting the fractional conversion of flow reactor. Therefore, maximizing the surface area of electrode within flow reactor should be set as a priority. (Pletcher & Walsh 1990, pp. 61–64.)

In the equations 8-10, it has been assumed that the electrode operates at optimal current distribution (Pletcher & Walsh 1991, p. 71). However, in practice the current distribution of three-dimensional electrode always has some non-uniformity (Pletcher & Walsh 1990, p.

129). Three-dimensional electrodes should have as isotropic porosity, electrical conductivity, and flow characteristics as possible to promote uniformity (Pletcher & Walsh 1990, p. 93; p. 126). Non-uniform current distribution results in several undesired effects, such as reduced current efficiency and thus uniformity is desired (Pletcher & Walsh 1990 p. 122). Non-uniform current distribution causes reaction to vary over the surface area of the electrode (Sun et al. 2019, p. 12).

The thickness of three dimensional electrodes should be considered. The current distribution will always be non-uniform parallel to the current flow, as the current densities increase towards the other electrode. (Pletcher & Walsh 1990 p. 131.) This is illustrated in Figure 30.

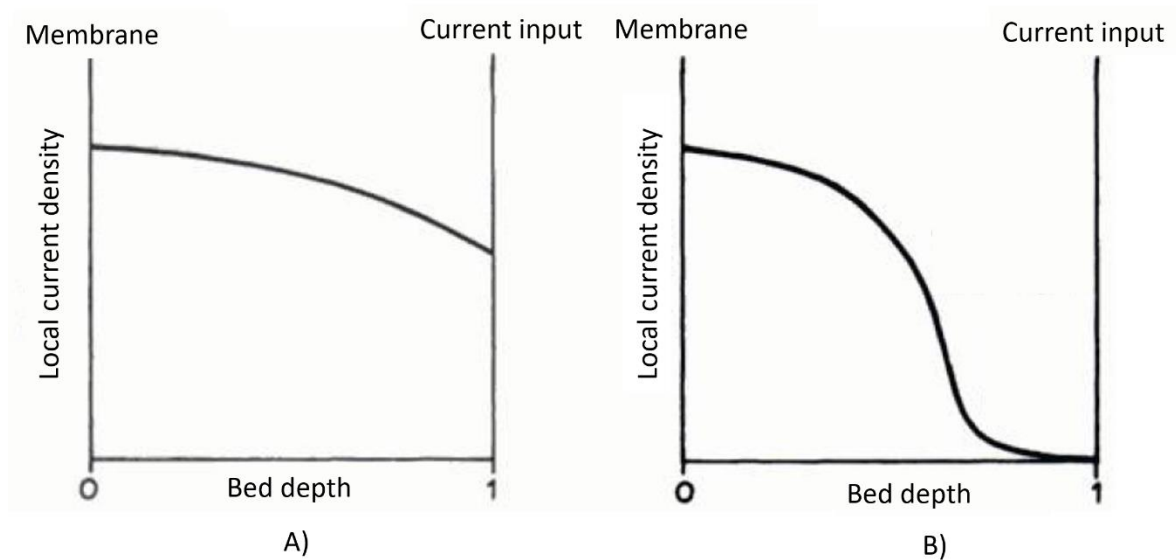


Figure 30. Current density through the 3D electrode thickness. a) Thin electrode, b) thick electrode. (Modified from Pletcher & Walsh 1990 p. 131)

As the Figure 30 depicts, the current distribution is relatively uniform through the electrode thickness if the electrode is relatively thin. As the electrode thickness increases, the current density drops to very small values near the current input. This non-uniformity through the electrode thickness can lead to some of its area to have negligible current and will not participate in the electron transfer, effectively reducing electroactive area. Therefore, it is important to consider the thickness, as inactive zones are to be avoided to maximize the A_e . (Pletcher & Walsh 1990 pp. 126–131.)

4.3.2 Material factors

Ideally electrode material should stay completely stable in the electrolyte. Complete stability however is often unachievable, leading to corrosion which directly affects electrodes lifetime. As electrode materials often do not demonstrate complete stability, electrode corrosion cannot be avoided in practice. Corrosion can be minimized choosing sufficiently stable electrode material for the used electrolyte. (Pletcher & Walsh 1990, p. 92.)

In the electrochemical gold recovery process, the electrolyte is hydrochloric acid solution (Kim et al. 2011, p. 208). Therefore, electrode material needs to stay as stable as possible in these conditions to minimize the electrode corrosion (Pletcher & Walsh 1990, p. 92; Zoski 2007, p. 111). Hydrochloric acid is one of the most difficult acids to handle and is very corrosive to most of the commonly used metals and alloys (Fontana 1987, p. 346). In previous studies, graphite or platinum electrodes have been used in this application (Kim et al. 2010, p. 96; Kim et al. 2011, p. 208).

5 DESIGN PROCESS OF THE ELECTRODE

The methods and process for the electrode designed in this thesis are presented in this chapter.

5.1 Defining requirements

The electrode was designed for the electro-chemical flow reactor, which is developed at LUT University for leaching of gold from electronic waste. Therefore, the electrode needs to fit in the place of the currently used electrode (Bilesan 2019). Electrode dimensions are presented in Figure 31.

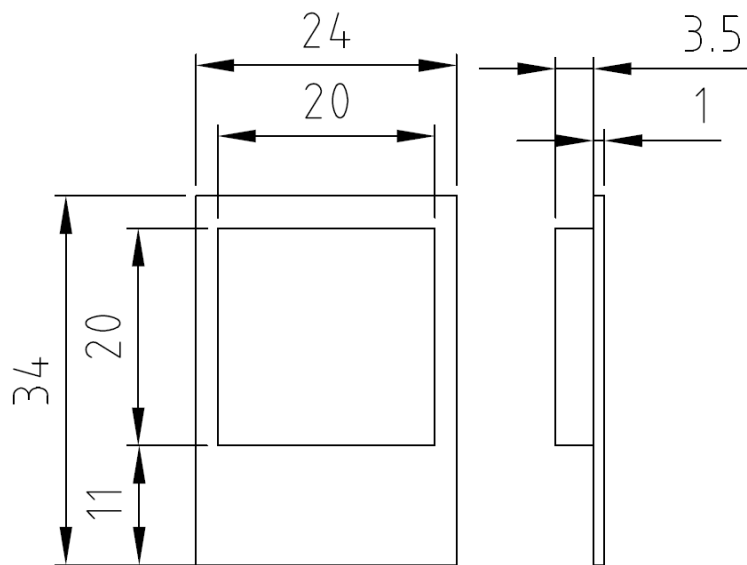


Figure 31. Electrode dimension for the electro-chemical flow reactor designed at LUT University (Modified from Bilesan 2019).

As the Figure 31 depicts, the electrode structure consists of two parts, the electrode and current collector. Current collector is required for securing electrically conductive contact (Pletcher & Walsh 1990, p. 93). This feature can be integrated to the porous electrode via AM, without the need for any adhesives which could lead to corrosion or passivation susceptibility (Arenas et al. 2017, p. 135).

Based on this and the findings in Chapter 4.3, requirements for the electrode can be summarized as presented in Table 2.

Table 2. Requirements for electrode.

Geometrical requirements	Material requirements
Large surface area	Electrical conductivity
Isotropic porosity	Stability in hydrochloric acid
Isotropic electrical conductivity	/
Isotropic flow characteristics	
Appropriate thickness	
Feature for securing electrically conductive contact	
Fit in the place of the currently used electrode	

As can be seen from Table 2, geometry for optimal electrode has multiple requirements, which can be controlled and manufactured by utilizing L-PBF (Arenas et al. 2017, p. 133). Large surface area is required to increase electrochemical activity and isotropic features and appropriate thickness are required to promote the uniformity of current distribution, resulting to constant reaction through the electrode (Pletcher & Walsh 1990, p. 126; Sun et al. 2019, p. 11). Additionally, the designed electrode needs to fit within the electrochemical flow reactor developed at LUT University.

As the electrodes are used in the gold separation process, electrode needs to be stable in hydrochloric acid solution. Material needs to be electrically conductive (Zoski et al. 2007, p. 111).

5.2 Material choice

The stability of the metal in hydrochloric acid was determined to be the most important material requirement in this thesis. Some pure metals, such as silver, platinum, tantalum and molybdenum demonstrate sufficient stability in hydrochloric acid (Fontana et al. 1987, pp. 347–350).

Wohler et al. (2019, p. 69) lists tantalum, platinum and silver as available AM materials. However, availability of these is limited. Platinum and silver are available for EOS Precious M 080 and Mlab Cusing metal AM systems (Concept Laser 2019; EOS 2019a; Wohlers et al. 2019, p. 357–364). Tantalum is commercially available for only one electron beam based PBF system (Wohlers et al. 2019, pp. 357–364).

Commonly available commercial L-PBF materials do not demonstrate required stability in hydrochloric acid environment. Manufactured electrodes will need to be coated with another metal to provide sufficient stability. Additively manufactured electrode has been coated, for example, in study by Arenas et al. (2017, pp. 133–137). In the study, electrode was manufactured from 316L and coated with nickel for electrochemical application (Arenas et al. 2017, p. 134). Therefore, the design of the electrode is done by considering 316L as build material to achieve the required geometry in this thesis. Electrode is designed to be coated with other metal to achieve the required stability. Stainless steels are commonly used as electrode materials, and thus fill the requirements for sufficient electrical conductivity (Pletcher & Walsh 1990, p. 92).

5.3 Modeling

To fulfill the requirements for large surface area and isotropic porosity, electrical conductivity, and flow characteristics, the lattice structure was utilized in the design of the electrode.

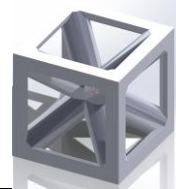
The modeling was started by modeling the design space, following the required dimension for the electrode presented in Figure 31. 3D modeling of the design space was done on Dassault Systemés' 3DEXPERIENCE platform. For the creation of lattice structure, SpaceClaim R2 software by ANSYS was utilized.

Larger surface area can be achieved with smaller feature sizes (Huang et al. 2017, p. 18176). Maximal surface area can be achieved by designing lattice structure with as small strut diameters and cell sizes as possible. Theoretical minimum strut diameter manufacturable with L-PBF is circa 0.15 mm. (Diegel et al. 2019, p. 137). This is in the same range as the minimum feature size value, 0.3 mm, for 316L given by material provider (EOS

2019b). Therefore, strut diameter of 0.3 mm and corresponding cell size of 1.2 mm were chosen for the lattice structure.

For the features to be isotropic, cell needs to be symmetrical in every direction. Different symmetrical cell shapes were compared to find cell with largest surface area. Each cell was modeled with size and strut thickness of 1.2 mm and 0.3 mm respectively. Cell comparison is presented in Table 3.

Table 3. Comparison of surface areas of different lattice cell shapes.

Lattice cell geometry				
Lattice cell number	1	2	3	4
Surface area [mm ²]	5.99	5.76	9.4	10.39

As Table 3 presents, the lattice cell number 4 has the highest surface area. Therefore, this cell shape is utilized in the electrode design carried out in this thesis to achieve the highest possible surface area. The CAD model was imported into lattice creation software and its solid section was converted into a lattice structure.

5.4 Simulation

Build process simulation was done for the electrode design to verify its manufacturability and to see if any excessive deformations are observed. Significant thermal deformations can lead to undesired defects affecting the electrode performance (Arenas et al. 2017, p. 135). For further comparison of predictions by different simulation methods, build process was done with two different software utilizing inherent strain and thermo-mechanical methods.

5.4.1 Thermo-mechanical simulation

The thermo-mechanical build process simulation was done on the Dassault Systemés' 3DEXPERIENCE platform. The software is based on Abaqus FE-solver and has an option to use simulation based on inherent strain or thermo-mechanical methods (Yang et al. 2019, p. 4). For this work, loosely coupled thermo-mechanical method was applied.

The platform and Abaqus offer features for feasible modeling of AM processes. These features include (Yang et al. 2019, p. 4; Zhang et al. 2019, p. 2):

- Progressive element activation, which allows elements to be partially or completely filled during the simulation. This enables the use of element meshes which do not match the actual powder layer thickness.
- A path intersection module, which is an algorithm used to recognize all the elements that the heat source passes through during each time increment.
- Progressive heating computations, which allows the heating to be computed by considering the actual path and power distribution of the heat source during each time increment.
- Machine information, which allows the actual manufacturing parameters, such as recoating time, laser scan path and material deposition to be accurately used for the simulation.

The electrode model was imported into the software in STL-format. As the electrode is composed of dense lattice structure, very fine FE-mesh is required to accurately represent the geometry. Simulating the whole lattice structure with very small elements would be unfeasible due to large nodal count in the simulation. Therefore, the lattice size was reduced to 3.5 mm x 3.5 mm x 3.5 mm block for the simulation. The current collector was excluded from the simulation due to its very simple geometry. This was deemed to be reasonable compromise to assess the manufacturability of the designed lattice structure in reasonable time. Another part representing the build plate was created and included in the simulation. This is important, as build plate considerably affects the thermal history prediction (Yang et al. 2019, p. 4). However, the build plate size can be reduced compared to the real one and still sufficiently account for the heat sink effect (Yang et al. 2019, p. 5). Modeled build plate dimensions were 20 mm x 20 mm x 10 mm.

Finite element mesh for the simulation was created on SIMULIA Additive Manufacturing Scenarios App. Lattice geometry and build plate were meshed using linear hexahedron DC3D8 elements. Element sizes used for build plate and lattice geometry were 1 mm and 0.05 mm, respectively. The two meshes were connected by applying tie contact. The FE-mesh is presented in Figure 32.

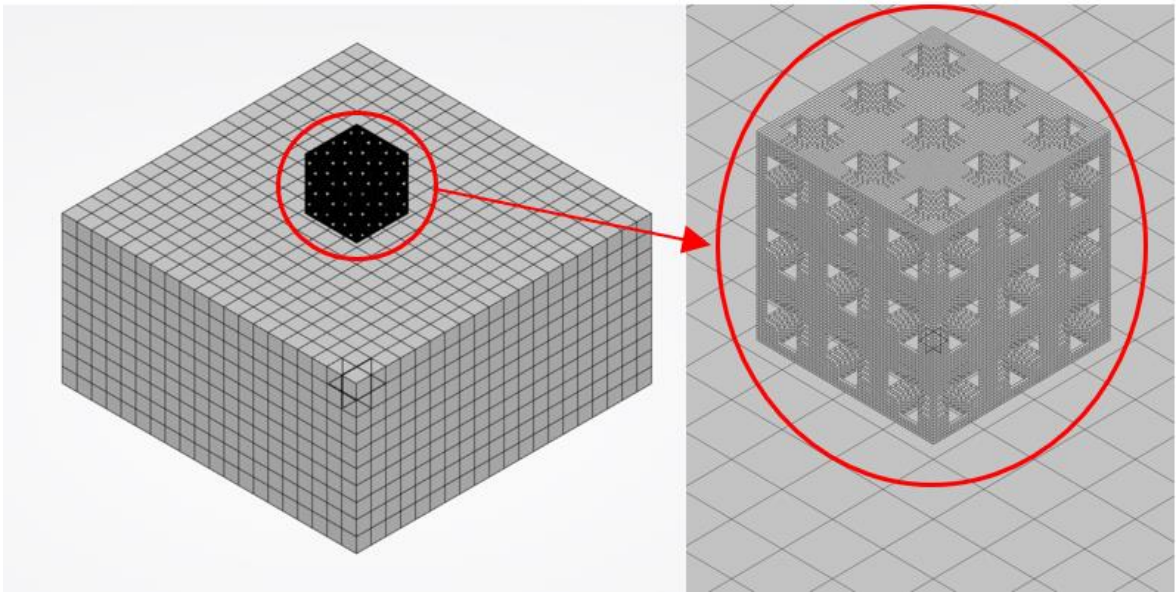


Figure 32. FE-mesh used for the simulation.

As the Figure 32 presents, FE-mesh does not correspond to actual powder layers and thus the partial element activation feature in the Abaqus was used to mitigate this difference. The used FE-mesh was identical for both thermal and mechanical simulations.

DELMIA Powder Bed Fabrication App within the platform was used to create slicing, recoating and laser beam information for the part. The process parameters used for the simulation are actual build parameters recommended by EOS and are presented in Table 4.

Table 4. Process parameters used in the simulation.

Layer thickness [mm]	0.02	-
Spot size [mm]	0.07	-
Recoating time [s]	10	-
	Infill	Contour
Laser Power [W]	195	110
Scan speed [mm/s]	1083	800
Hatch spacing [mm]	0.09	0.09
Scanning strategy	Stripes	Two contours
Stripe width [mm]	5	-
Stripe overlap [mm]	0.12	-
Scan rotation [°]	67	-
Build plate preheating [°C]	80	-

The process parameters presented in Table 4 were input into the software and toolpath data was created accordingly. The geometry with build plate, alongside with the visualization of laser scan path is presented in Figure 33.

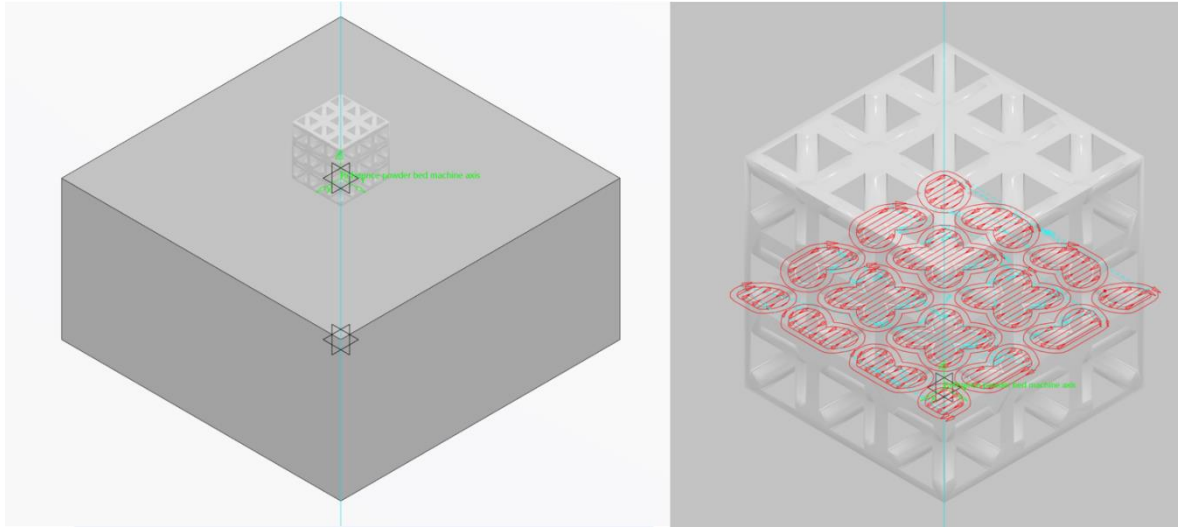


Figure 33. Lattice geometry on build plate and visualization of laser scan path.

As the Figure 33 shows, the created laser scan path accurately represents the actual scan path of the laser beam during the build process.

Material used for the build simulation was 316L stainless steel. Due to thermal simulation step, some temperature-dependent material properties are required as an input for the simulation. Material density, solidus and liquidus temperatures, latent heat of fusion, absorption coefficient and Poisson's ratio were set as temperature independent. Thermal conductivity, specific heat capacity, Young's modulus, and coefficient of thermal expansion are set as temperature dependent. Additionally, the plasticity of the material is set as temperature independent, as the plastic behavior shows only a small dependency on temperature due to the range of temperatures experienced during single time increment (Yang et al. 2019, p. 5). The material properties were extracted from literature and are presented in Appendix I.

For the simulation, thermal analysis was first conducted to predict the thermal history of the part due to the build process. For this analysis, a single transient heat transfer analysis step, with duration slightly longer than total build of the part is conducted. The added time allows

the part to cool down to room temperature after the build is complete. Time increments during the step were set to include spreading and heating of one layer during each time increment. The laser beam is modeled as a moving concentrated point heat source. As the parameters and scan paths are considered through the features available in Abaqus, the energy input is distributed accordingly in each time increment. Initial temperatures for the part and build plate were set to 26°C. Heat loss was considered through convection and radiation, as presented in equations 2 and 3, respectively. Heat transfer coefficient, h , was set to 18 W/m²K and emissivity, ϵ , to 0.25, as deemed suitable for same material by Deering (2018, p. 5). The preheating of the build platform was modeled by applying thermal boundary condition of 80 °C on the bottom of the build plate.

Modeling of material deposition during the simulation is important, as it has large effect on the thermal behavior of the system (Yang et al. 2019, p. 6). The material deposition was modeled by applying element birth method available in Abaqus, allowing elements to be added to the model at each time increment.

For mechanical analysis, static mechanical step was used, with time step corresponding to the thermal analysis. The thermal history was imported into the mechanical analysis and developing stresses and deformations were calculated through thermal expansion. Initial temperature for the lattice geometry was set to temperature, which represents the temperature above which thermal straining induces negligible stresses. This temperature was set to 750°C, as deemed suitable for similar material by Yang et al. (2019, p. 9). Initial temperature for build plate was set to 26°C, and fixed boundary condition was set on its bottom.

5.4.2 Inherent strain analysis

The analysis utilizing inherent strain method was conducted by ANSYS Additive Print software. Same simplified lattice model was used for inherent strain simulation, as was used for the thermo-mechanical simulation.

The part was imported into the software in STL-format. The FE-mesh was generated by using linear hexahedron DC3D8 element type, with a size of 0.05 mm. The FE-mesh is presented in Figure 34.

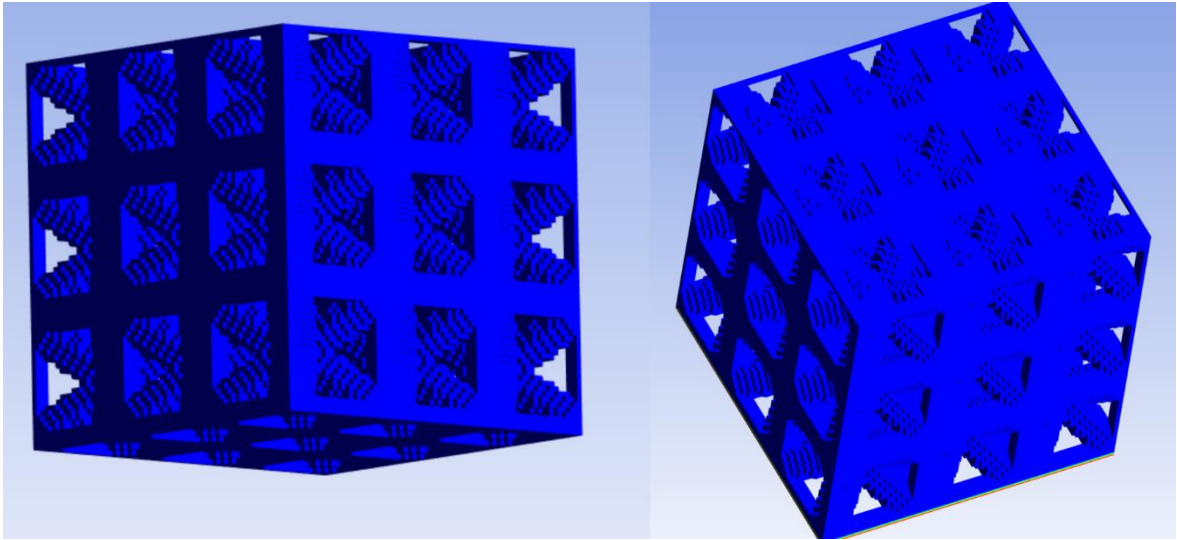


Figure 34. FE-mesh used in inherent strain simulation.

As it can be seen from Figure 34, FE-mesh is similar to one used for thermo-mechanical analysis. As no thermal simulation step is required in inherent strain method, only strength properties of materials in ambient temperature are required for the analysis (Bugatti et al. 2019, p. 332). The Young's modulus, Poisson's ratio and yield strength in 21°C listed in Appendix I were input for the simulation model.

For the simulation, single mechanical step with inherent strain being introduced for each element during their activation was used. The pre-calibrated value in the software for the inherent strain was used, without any further calibration.

6 RESULTS AND DISCUSSION

In this chapter, the results of the literature study and case part are presented.

6.1 DfAM process

An updated DfAM process chart was formed based on findings from literature review. Design for additive manufacturing is multifaceted design optimization process, which can be described as presented in Figure 35.

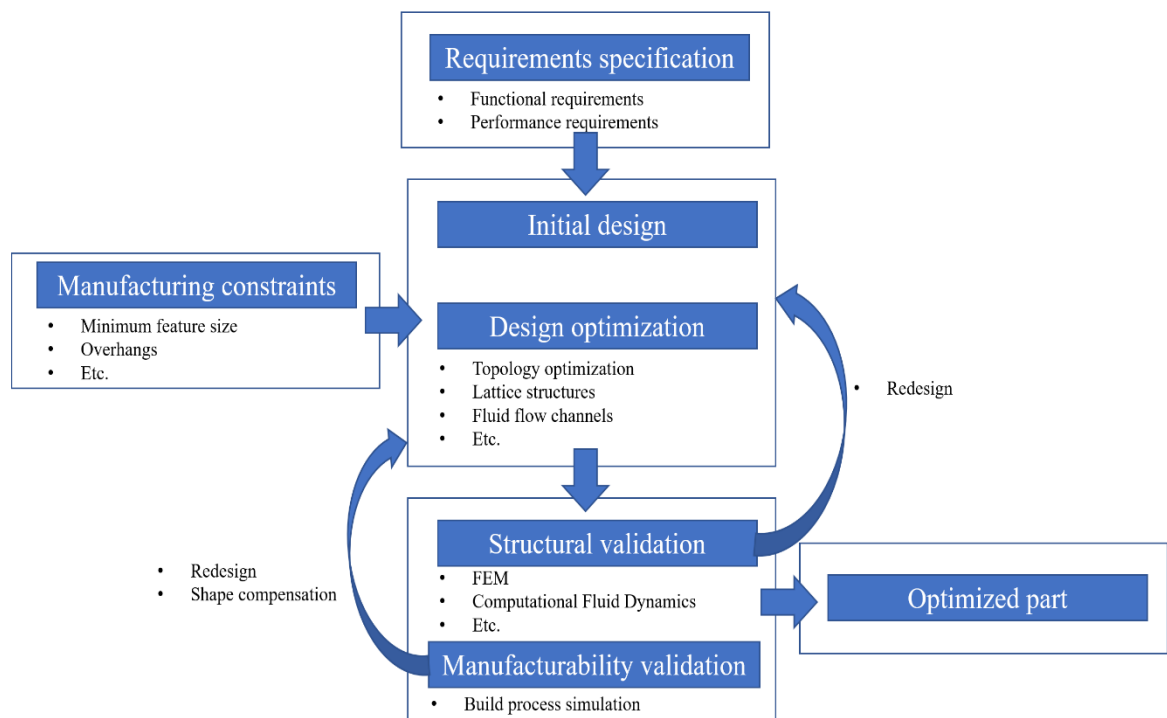


Figure 35. DfAM process chart.

As the Figure 35 depicts, DfAM process is started by first defining the requirements for the design case. After this, initial design fulfilling the requirements is design. For the initial design, aspects such as possible part consolidation should be considered. Various design optimization procedures, such as topology optimization or lattice generation, can then be carried out in order to add value to the design. L-PBF process has its constraints with for example overhangs and minimum manufacturable feature sizes and these should be considered in the design process. After design is optimized, validation phase is conducted.

During this phase it is validated, that the designed part performs as specified by the initially determined requirements. This can be done for example, by applying FEM or CFD calculations depending on application. This chart differs from previously introduced ones by including the manufacturability validation step. In this step the manufacturability of the design can then be validated through build process simulations. If validations fail, changes to the design are required. Additionally, shape compensation can be used to manufacture part closer to the intended shape based on build process simulation results. After these steps are successfully carried through, optimized part is then ready to be manufactured.

6.2 Electrode design

An optimized electrode was designed by applying DfAM chart presented in Figure 35, by considering the requirements, limitations and possibilities defined in the case study part of this thesis. The electrode geometry follows the requirement specifying it needs to fit in the flow reactor designed at LUT University. Therefore, only the area of the lattice was possible to be subjected for further optimization. Designed electrode geometry is presented in Figure 36. Designed electrode structure.

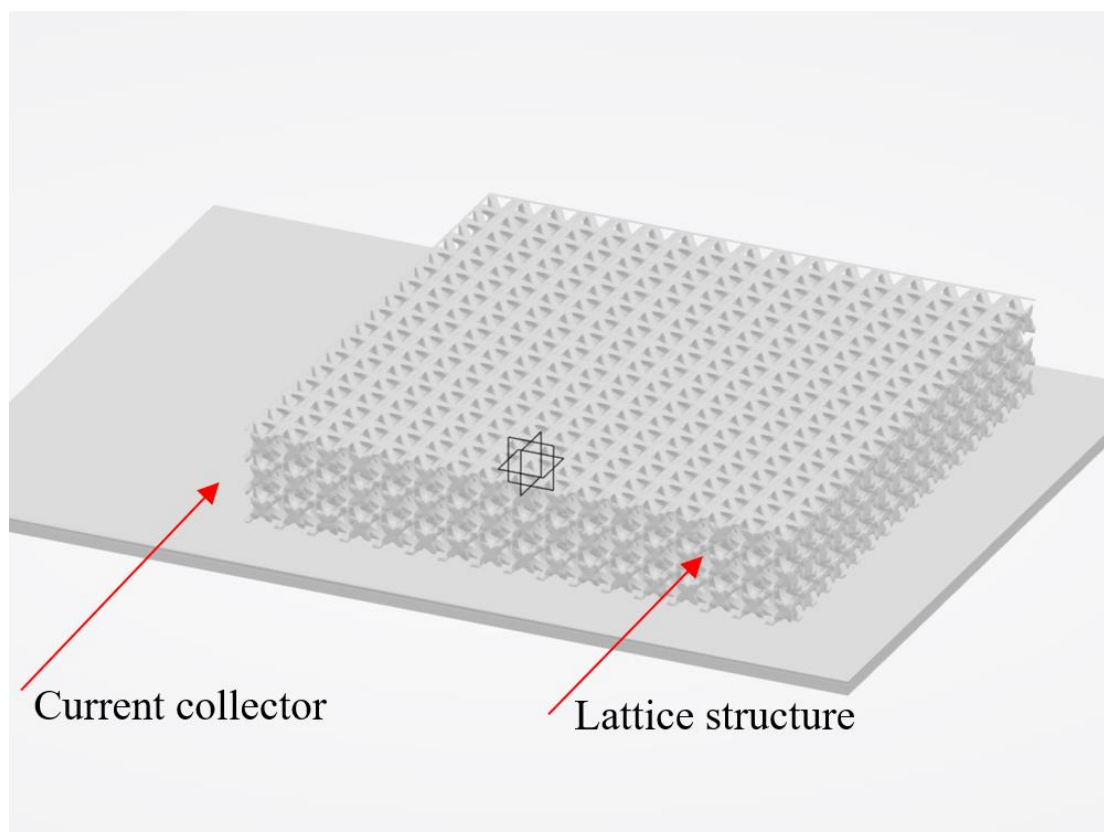


Figure 36. Designed electrode structure.

As the Figure 36. Designed electrode structure. shows, the electrode is composed of very dense lattice structure. The most important factor affecting three-dimensional electrodes performance in flow reactor was determined to be its surface area. Large surface area was achieved by using lattice strut and cell sizes corresponding to smallest feature sizes manufacturable with L-PBF. Lattice geometry was also modeled to have cell geometry with maximized surface area. The surface area of the lattice part is approximately 5800 mm².

Additionally, the electrode lattice is designed to be symmetrical in every direction. This ensures isotropic porosity across the electrode structure, enhancing the isotropy of its flow and electrical conductivity properties. This promotes the uniformity of current distribution within the electrode, which is critical to achieve optimal performance during the electrochemical process.

The current collector and lattice structure are manufactured from same material as a single part. This ensures uniform connection between the two, as no additional adhesives or welds are required. This feature also promotes the uniformity of the current distribution (Arenas et al. 2017, p. 135).

6.3 Build process simulations

Build process simulation was done by applying two different methods with two different software. Results are presented in this chapter. The differences of used simulation methods are summarized in Figure 37.

	Inherent strain		Thermo-mechanical			
Input	Material mechanical properties in room temperature	Strain values	Temperature dependent material properties	Process parameters		
Simulation steps	Mechanical simulation		Thermal simulation	Mechanical simulation		
Results	Local plasticity induced by laser beam considered	Geometry specific temperature history ignored	Local plasticity induced by laser beam ignored	Geometry specific temperature history considered		
Additional procedures	Strain calibration					
Pros	Relatively short simulation times		Change in material or parameters can be considered with changing inputs	Calibration not required		
Cons	Need for calibration with each material, parameter set etc.	Possible inaccuracies due to negligence of geometry specific temperature history	Relatively long simulation times	Determining temperature dependent material properties can be difficult	Possible inaccuracies due to negligence of local plasticity	Process parameters not always available

Figure 37. Differences of inherent strain and thermo-mechanical simulation method.

As the Figure 37 presents, both process simulation methods have their pros and cons. The required inputs, simulation steps and other procedures vary between the methods, because approximation of the L-PBF process is done differently.

6.3.1 Thermo-mechanical simulation

To assess the manufacturability and usability of the lattice structure, displacement values were plotted from the simulation results. Displacement contour plot predicted by thermo-mechanical analysis is presented in Figure 38.

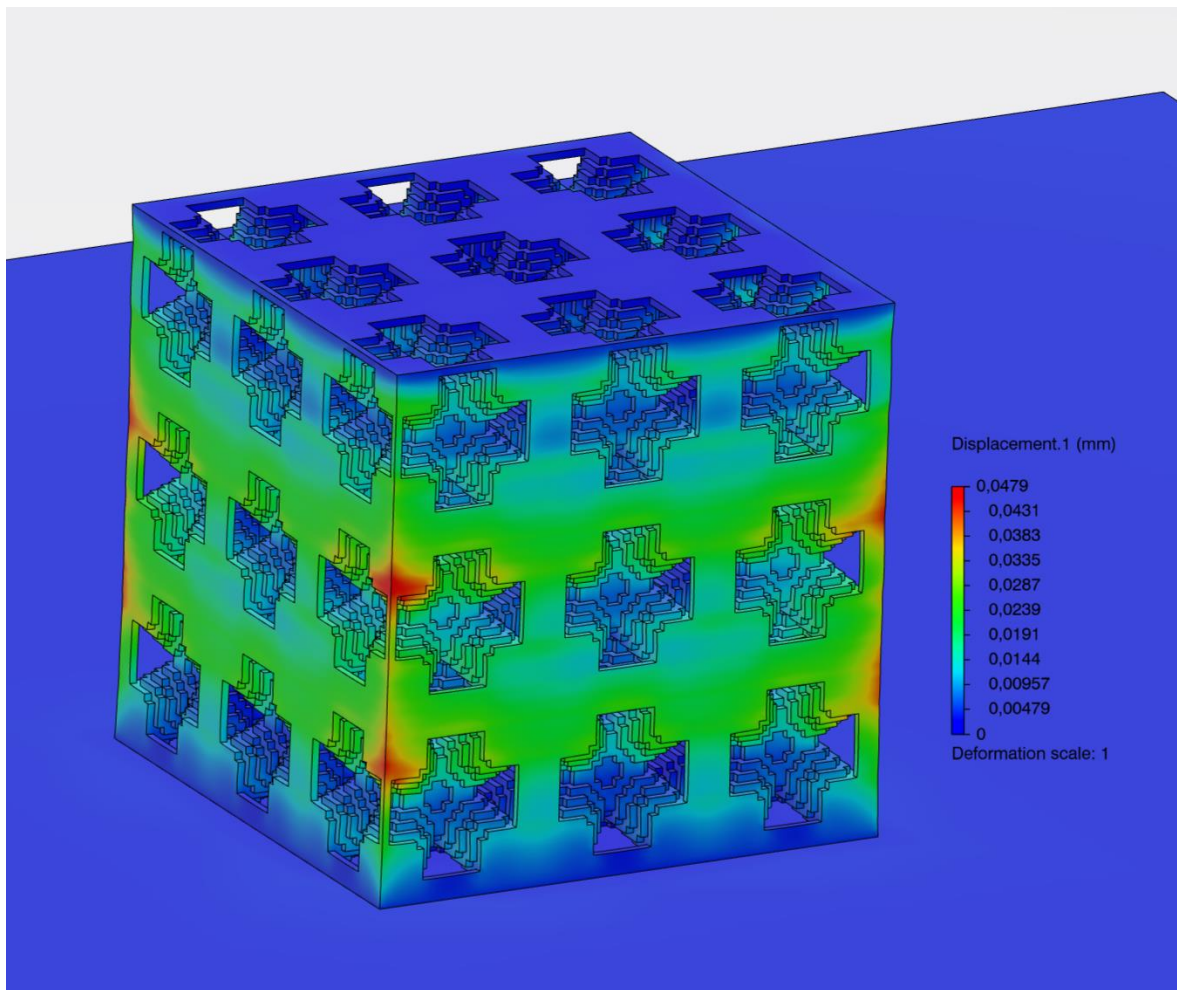


Figure 38. Displacement contour plot predicted by thermo-mechanical analysis.

Figure 38 shows that maximum displacements are circa 0.048 mm. Maximum displacements are located in relatively small areas in the outer corners of the simulated lattice structure. Smaller deformations can be observed around the lattice structure, especially on its outer facets, with values less than 0.010 mm. Inside the lattice structure, displacements are even smaller.

The possibility of recoater collision was also assessed from the simulation results. As the displacements were small, no potential areas for recoater collision were identified.

6.3.2 Inherent strain simulation

From the inherent strain analysis, displacement values were plotted. Displacement contour plot predicted by this analysis is presented in Figure 39.

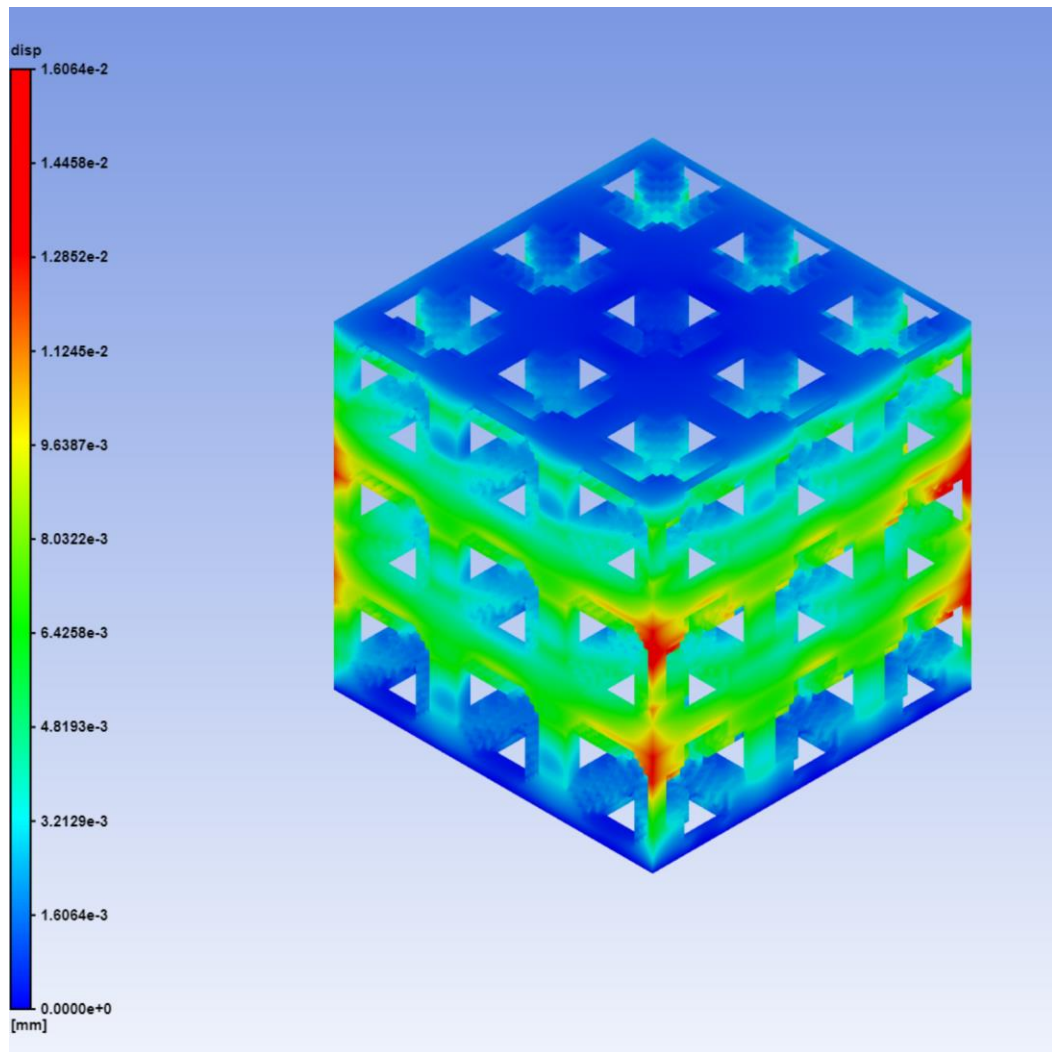


Figure 39. Displacement contour plot predicted by inherent strain analysis.

Figure 39 illustrates that maximum displacements are circa 0.016 mm. Maximum displacements are located in relatively small areas (red areas in Figure 39) in the outer corners of the simulated lattice structure. Smaller deformations can be observed around the lattice structure, especially on its outer facets, with values less than 0.010 mm. Inside the lattice structure, displacements are even smaller.

The possibility of recoater collision was also assessed from the simulation results. As the displacements were small, no potential areas for recoater collision were identified.

6.3.3 Discussion

Predicted values by two methods vary with maximum value estimate of thermo-mechanical method being three times larger. However, the predicted trend of displacements is very similar as can be observed from Figures 38 and 39.

For the inherent strain method analysis, pre-calibrated values in the software were used for the simulation. When using inherent strain method, strain value should always be calibrated for used machine, parameter set and material (Gouge et al. 2019, p. 2). Because this procedure was not conducted for this work, the accuracy of inherent strain analysis is compromised. This could partly be a reason for differing predictions of inherent strain and thermo-mechanical simulations.

The two used methods approximate the L-PBF process very differently for the simulation. Inherent strain method assumes that the strain developed during the manufacturing process is uniform in all layers. Because of this, the effect of part geometry on the thermal history is not considered. In thermo-mechanical simulation, multiple layers and laser passes are usually included in single time step. Therefore, this method does not capture the local plasticity induced by the laser beam. These differences could also be affecting the difference of the predictions.

The deformations of the lattice predicted by both methods is minimal. This indicates that the lattice should be close to the intended shape after manufacturing. Therefore, its structure should still be reasonably uniform and thus fill the requirement for uniform structure and porosity.

Structure size was reduced for the simulation to make nodal count more reasonable, while accurately capturing the geometry with FE-mesh. Because of this approximation, the predicted values might not accurately reflect the ones achieved when manufacturing the whole structure. However, it is reasonable to assume that the manufacturability and very small deformations observed from the results would still hold for the full-size lattice to acceptable degree.

Voxel meshing approach was used for the meshing of the lattice geometry. Therefore, the geometry was approximated by voxels corresponding to the used element size. While used element size was very small and representation of the geometry with voxel mesh is quite close to the original, some discrepancy still exists and might affect the accuracy of the results.

7 CONCLUSIONS

Designing parts to be manufactured with L-PBF opens new opportunities, as many of the limitations inherent to the traditional manufacturing processes are mitigated. Therefore, parts can be designed to be specifically optimized for certain application, resulting in high-performance components. However, this manufacturing process also has its own limitations and the design process requires deep understanding of both the limitations and possibilities.

The thesis was carried out in the research group of Laser Material Processing and Additive Manufacturing of LUT University as a part of ReGold-AM project funded by Academy of Finland. The project is done in co-operation with research group of Hydrometallurgy for Urban Mining. The aim of the project is to construct novel electrochemical reactors for gold recovery purposes by leveraging possibilities offered by AM. The project lasts from 01.09.2019 to 31.08.2023.

The aim of this thesis was to determine what needs to be considered in the DfAM process. The goal was to recognize the design process, what new design opportunities does the manufacturing method offer, what are its limitations and what tools are required to successfully design AM parts. Literature review part of the thesis answers these questions, while the case part was done to demonstrate these aspects by designing optimized electrode for electrochemical gold separation process.

DfAM requires new design tools to be adapted. As geometries get significantly more complex through optimization, traditional CAD tools become too limited. Design tools for topology optimization, lattice generation and advanced modeling become necessary to fully take advantage of the design possibilities.

Another important design tool for AM is the process simulation. As L-PBF is expensive and slow manufacturing process, build failures can be intolerable. Process simulation software allow designer to verify the manufacturability of the part before the actual manufacturing, to make sure the build process will complete, and the part will be usable. (Diegel et al. 2019, pp. 76–77.)

Various methods for the build process simulation on part scale have been developed. All these methods approximate the actual process to produce results in reasonable timeframe, with each having some strengths and weaknesses. Inherent strain approach is the most commonly used simulation method in commercial software (Gouge et al. 2019, p. 2). It uses measured data from physically printed test part or micro-scale simulation to calculate strain values. This data is then mapped on part scale model without the need for thermal simulation step. Because of this, the effect of part geometry on the thermal history is not considered in this method. In thermo-mechanical approaches, thermal and mechanical simulations are loosely coupled to capture the development of residual stresses within the part. Heat input is calculated for each time step and elements are activated accordingly. Because multiple layers and laser passes are usually included in single time step, this method does not capture the local plasticity induced by the laser beam. Multi-scale approach effectively combines these two methods, by first determining plastic deformations from small scale model, and then introducing data to the part scale mechanical analysis, along with the data from part scale thermal analysis. Different methods to simulate the deposition of layers and to reduce the number of needed elements, such as progressive element activation and mesh coarsening, have also been developed. Experience and experiments are required to determine appropriate method along with other factors such as element size and time step to accurately capture real life phenomena with simulation tools in reasonable times.

The DfAM process was demonstrated by designing optimized electrode structure to be used for electrochemical gold separation process. Three-dimensional electrodes used in flow reactors benefit from increased surface area and uniform, well controlled porosity. These features can be achieved through use of lattice structures, which can be generated through specific design tools and manufactured with L-PBF. The structure of the lattice can be optimized by considering the limitations of L-PBF together with the requirements to achieve highest possible surface area and uniform flow properties.

The manufacturability of the lattice was assessed by applying build process simulations. Two different methods, thermo-mechanical and inherent strain, were used to compare the approaches and highlight their differences. The magnitude of predicted values by both methods differ only slightly, while the trends also match very closely. Both methods estimate

similar, very limited deformations resulting from the manufacturing process. This indicates that the optimized electrode geometry is well manufacturable with L-PBF.

8 FURTHER STUDIES

As the electrode was optimized based on literature review, its performance was not tested experimentally in this work. Therefore, further study would be to experimentally validate the electrodes performance, and optimize the structure further, if necessary.

The build process simulations used in this work were not validated experimentally. In the future studies, the results predicted by the used methods could be verified by comparing them to experimentally built components. Also, the calibration procedures for inherent strain method could be done to correctly account for used build parameters. The predictions of thermo-mechanical and inherent strain methods could then be reasonably compared. Additionally, the multi-scale simulation approach could also be compared to the two methods used in this work. Simulation times and accuracies of each method could then be studied to find optimal method to be used in different cases.

Build process simulations include a lot of variables, such as used element type, size and time increment. Effect of these, and other, variables could be studied to assess their effect on simulation times and accuracies.

Current commercially available materials for L-PBF do not demonstrate sufficient stability in hydrochloric acid. Printability of materials, such as tantalum, molybdenum and platinum could be studied in the future to allow manufacturing of complex electrode shapes without need for additional coating to provide stability.

LIST OF REFERENCES

Afkhami, S., Dabiri, M., Alavi, S.H., Björk, T. & Salminen, A. 2019. Fatigue characteristics of steels manufactured by selective laser melting. *International Journal of Fatigue* 122. Pp. 72-83.

Arenas, L.F., Ponce de León, C. & Wals, F.C. 2017. 3D-printed porous electrodes for advanced electrochemical flow reactors: A Ni/stainless steel electrode and its mass transport characteristics. *Electrochemistry Communications* 77. Pp. 133-137.

Bard, J.A. & Faulkner L.R. 2001. *Electrochemical Methods, Fundamentals and Applications*. Second Edition. New York: John Wiley & Sons, Inc. 850 p.

Bilesan, R. 2019. RE: Questions of dimensions of electrodes [private email]. Receiver: atte.heiskanen@lut.fi. Sent: 4.12.2019 12:35 o'clock (GMT +0200)

Brandt, M. 2017. *Laser additive manufacturing: Materials, design, technologies, and applications*. Amsterdam: Elsevier. 479 p.

Bugatti, M. & Semeraro, Q, 2018, Limitations of the inherent strain method in simulating powder bed fusion process. *Additive Manufacturing* 23. Pp. 329-346

Chen, Q., Liang, X., Hayduke, D., Liu, J., Cheng, L., Oskin, J., Whitmore, R. & To, A.C. 2019. An inherent strain based multiscale modeling framework for simulating part-scale residual deformation for direct metal laser sintering. *Additive Manufacturing* 28. Pp. 406-418

Concept Laser 2019. Mlab cusing. [Concept laser webpage]. [Referred 17.10.2019].

Available:

https://www.conceptlaser.de/fileadmin/Machine_brochures/CL_Mlab_cusing_DS_EN_A4_2_v1.pdf

Das, P., Chandran, R., Samant, R & Anand, S. 2015. Optimum Part Build Orientation in Additive Manufacturing for Minimizing Part Errors and Support Structures. *Procedia Manufacturing* 1. Pp. 343-354.

Deering, R.A. 2018. Additive Manufacturing Part Level Distortion Sensitivity Analysis within Abaqus on a Thin-walled, Tubular Structure. *Science in the Age of Experience 2018 Proceedings*. Pp. 1-14

Denglinger, E.R., & Michaleris, P. 2016. Effect of stress relaxation on distortion in additive manufacturing process modeling. *Additive Manufacturing* 12. Pp. 51-59.

Diegel, O., Nordin, A. & Motte, D. 2019. *A Practical Guide to Design for Additive Manufacturing*. Singapore: Springer. 226 p.

EOS. 2019a. PRECIOUS M 080. [EOS webpage]. [Referred 17.10.2019]. Available: <https://www.eos.info/precious-m-080>

EOS. 2019b. Materials for Metal Additive Manufacturing. [EOS webpage]. [Referred 17.10.2019]. Available: <https://www.eos.info/material-m>

Fontana, M.G. 1987. *Corrosion Engineering*. Third edition. New York: McGraw-Hill Book Company. 556 p.

Gebisa, A.W. & Lemu, H.G. 2017. Design for manufacturing to design for Additive Manufacturing: Analysis of implications for design optimality and product sustainability. *Procedia manufacturing* 13. Pp. 724-732

Huff, R & Wohlers, T. 2019. Redesigning for Additive Manufacturing: Serial production of a new fuel swirler for Siemens gas turbine. *Metal Additive Manufacturing* Vol. 5 No. 3. Autumn/Fall 2019. Pp. 169-172

Gibson, I., Rosen, D. & Stucker, B. 2015. Additive Manufacturing Technologies. 3D Printing, Rapid Prototyping, and Direct Digital Manufacturing. Second Edition. New York: Springer. 498 p.

Gouge, M., Denlinger, E., Irwin, J., Li, C. & Michaleris, P. 2019. Experimental validation of thermo-mechanical part-scale modeling for laser powder bed fusion. Additive Manufacturing 29. Pp. 1-17.

Gouge, M. & Michaleris P. 2018. Thermo-mechanical modeling of additive manufacturing. Offord: Butterworth-Heinemann, and imprint of Elsevier. 275 p.

Graziosi, S., Rosa, F., Casai, R., Solarino, P., Maurizio, V. & Bordegoni, M. 2017. Designing for Metal Additive Manufacturing: a case study in the professional sports equipment field. Procedia Manufacturing 11. Pp. 1544-1551

Gu, D. 2015. Laser Additive Manufacturing of High Performance Materials. Berlin: Springer. 311 p.

Hodge, N.E., Ferencz, R.M. & Vignes R.M. 2016. Experimental comparison of residual stresses for a thermomechanical model for the simulation of selective laser melting. Additive Manufacturing 12. Pp. 159-168.

Huang, X., Chang, S., Siang, W., Lee, W., Ding, J & Xue, J.M. 2017. Three-dimensional printed cellular stainless steel as high-activity electrode for oxygen evolution. Journal of Materials Chemistry A 5. Pp. 18176-18182.

ISO/ASTM 52910. 2018. Additive manufacturing – Design – Requirements, guidelines and recommendations. 1st edition.

Kim, E., Kim, M., Lee, J., Yoo, K. & Jeong, J. 2010. Leaching behavior of copper using electro-generated chlorine in hydrochloric acid. Hydrometallurgy 100. Pp. 95-102.

Kim, E., Kim, M., Lee, J. & Pandey, B.D. 2011. Selective recovery of gold from waste mobile phone PCBs by hydrometallurgical process. *Journal of Hazardous Materials* 198. Pp. 206-215.

Klingaa, C.G., Dagmen, T., Baier, S., Mohanty, S. & Hattel, J.H. 2019. Build orientation effects on the roughness of SLM channels. Joint Special Interest Group meeting between euspen and ASPE Advancing Precision in Additive Manufacturing. Pp. 1-4.

Kruth, J.P., Froyen, L., Van Vaerenbergh, J., Mercelis, P., Rombouts, M. & Lauwers, B. 2004. Selective laser melting of iron-based powder. *Journal of Materials Processing Technology* 149. Pp. 616-622.

Leach, R.K., Bourell, D., Carmignato, S., Donmez, A., Senin, N. & Dewulf, W. 2019. Geometrical metrology for metal additive manufacturing. *CIRP Annals – Manufacturing Technology*. Pp. 1-24

McKee, H.J. & Porter, J.G. 2017. Lessons Learned in Part Design from Topology Optimization through Qualification. *Science in the Age of Experience 2017 Proceedings*. Pp. 54-70.

Milewski, J.O. 2017. *Additive Manufacturing of Metals. From Fundamental Technology to Rocket Nozzles, Medical Implants, and Custom Jewelry*. Cham: Springer. 343 p.

Mishra, A., Shoesmith, D. & Manning, P. 2017. Materials for Use in Concentrated Hydrochloric Acid. *Corrosion* 73. Pp. 68-76.

Neiva, E., Badia, S., Martín, A.F. & Chiumenti, M. 2019. A scalable parallel finite element framework for growing geometries. Application to metal additive manufacturing. *International Journal for Numerical Methods in Engineering* 119. Pp. 1098-1125.

NIST. 2018. AMD2018-01 Description. [web document]. Available: <https://www.nist.gov/ambench/amb2018-01-description>

nTopology. 2019a. Element Pro Case Study: F1 Brake Pedal. [web document]. Available: https://ntopology.com/wp-content/uploads/2019/02/Brake_Pedal_Case_Study.pdf

nTopology. 2019b. nTop Platform for Medical Devices. [web document]. Available: <https://ntopology.com/wp-content/uploads/2019/05/nTop-Platform-for-Medical-Devices.pdf>

Oh, Y., Zhou, C. & Behdad, S. 2018. Part decomposition and assembly-based (Re) design for additive manufacturing: A review. *Additive Manufacturing* 22. Pp. 230-242.

Orquéra, M., Campocasso, S., & Millet, D. 2017. Design for additive manufacturing method for mechanical system downsizing. *27th CIRP Design 2017*. Pp. 223-228.

Panda, B.K. & Sahoo, S. 2019. Thermo-mechanical modeling and validation of stress field during laser powder bed fusion of AlSi10Mg build part. *Results in Physics* 12. Pp. 1372-1381.

Pletcher, D & Walsh, F.C. 1990. *Industrial Electrochemistry*. Second Edition. New York: Chapman and Hall. 661 p.

Pletcher, D & Walsh, F.C. 1991. Chapter 3: Three-dimensional electrodes. *Electrochemistry for a cleaner environment*. Pp. 51-100.

SFS-EN ISO/ASTM 52900:en. 2017. Additive manufacturing. General principles. Terminology (ISO/ASTM 52900:2015). Helsinki: Finnish Standards Association SFS. 25 p.

Simson, T., Emmel, A., Dwars, A. & Böhm, J. 2017. Residual stress measurements on AISI 316L samples manufactured by selective laser melting. *Additive Manufacturing* 17. Pp. 183-189.

SLM Solutions 2019. SLM METAL POWDER [SLM Solutions webpage]. [Referred 17.10.2019]. Available: <https://www.slm-solutions.com/en/products/accessories-consumables/slmr-metal-powder/>

- Snyder, J.C., Stimpson, C.K., Thole, K.A. & Mongillo, D.J. 2015. Build Direction Effects on Microchannel Tolerance and Surface Roughness. *Journal of Mechanical Design* 137. Pp. 1-7.
- Sun, X., Lin, H., Zhang, C., Huang, X., Jin, J. & Di, S. 2019. Electrosynthesized nanostructured polypyrrole on selective laser melted titanium scaffold. *Surface & Coatings Technology* 370. Pp. 11-17.
- Valencia, J.J & Queded, P.N. 2008. Thermophysical Properties. *ASM Handbook, Volume 15: Casting*. Pp. 468-481
- Williams, R.J., Davies, C.M. & Hooper, P.A. 2018. A pragmatic part scale model for residual stress and distortion prediction in powder bed fusion. *Additive Manufacturing* 22. Pp. 416-425.
- Wohlers, T., Campbell, I., Diegel, O., Hugg, R., Kowen, J., Bourell, D.L. & Ismail, F. 2019. Wohlers report 2019. 3D printing and additive manufacturing state of the industry. 369 p.
- Yang, Y., Allen, M., London, T. & Oancea, V. 2019. Residual Strain Predictions for a Powder Bed Fusion Inconel 625 Single Cantilever Part. *Integrating Materials and Manufacturing Innovation*. Pp. 1-11.
- Yang, L., Hsu, K., Baughman, B., Godfrey, F., Medina, F., Menon, M. & Wiener, S. 2017. *Additive Manufacturing of Metals: The Technology, Materials, Design and Production*. Cham: Springer. 168 p.
- Yang, S., Zhao, Y.F. 2015. Additive manufacturing enabled design theory and methodology: a critical review. *The International Journal of Advanced Manufacturing Technology* 80. Pp. 327-342.

Zhang, L., Reutzel, E.W. & Michaleris, P. 2004. Finite element modeling discretization requirements for the laser forming process. *International Journal of Mechanical Sciences*. Pp. 623-637.

Zhang, Q., Xie, J., Gao, Z., London, T., Griffiths, D. & Oancea, V. 2019. A metallurgical phase transformation framework applied to SLM additive manufacturing process. *Materials and Design* 166. Pp. 1-18.

Zoski, C.G. 2007. *Handbook of Electrochemistry*. Amsterdam: Elsevier. 809 p.

Material properties of 316L used for thermo-mechanical simulation

Property	Value	Temperature [°C]	Source
Density [g/cm³]	7.95	-	Valencia & Qusted 2008, p. 475
Solidus temperature [°C]	1384.85	-	Valencia & Qusted 2008, p. 475
Liquidus temperature [°C]	1449.85	-	Valencia & Qusted 2008, p. 475
Latent heat of fusion [J/kg]	260000	-	Valencia & Qusted 2008, p. 475
Poisson's ratio	0.27	-	Deering 2018, p. 5
Concudctivity [W/m/°C]	14.89	0	Deering 2018, p. 5
	14.89	20	
	15.79	27	
	16.61	77	
	18.28	127	
	19.77	227	
	21.21	327	
	22.59	427	
	23.99	527	
	25.33	627	
	26.58	727	
	27.81	827	
	28.18	927	
	30.34	1027	
	31.55	1127	
	32.7	1227	
	32.4	1327	
	32.5	1400	
Young's Modulus [Mpa]	195121	21	Deering 2018, p. 5
	189605	93	
	186158	149	
	182021	204	
	178574	260	
	174437	315	
	170989	371	
	166163	426	
	162026	482	
	157200	537	
	151684	593	

Material properties of 316L used for thermo-mechanical simulation

Property	Value	Temperature [°C]	Source
Young's Modulus [Mpa]	146168	649	Deering 2018, p. 5
	139963	704	
	132379	760	
	124795	815	
Thermal expansion coefficient	1.46e-05	10	Deering 2018, p. 5
	1.46e-05	20	
	1.48e-05	27	
	1.52e-05	77	
	1.56e-05	127	
	1.63e-05	227	
	1.59e-05	327	
	1.74e-05	427	
	1.79e-05	527	
	1.83e-05	627	
	1.87e-05	727	
	1.9e-05	827	
	1.93e-05	927	
	1.95e-05	1027	
	1.96e-05	1127	
	1.98e-05	1227	
Specific heat capacity [J/kg°C]	503	25	Deering 2018, p. 5
	518	100	
	538	200	
	558	300	
	578	400	
	598	500	
	618	600	
	638	700	
	658	800	
	678	900	
	698	1000	
	718	1100	
	738	1200	
	758	1300	
	778	1400	
	788	1450	

Material properties of 316L used for thermo-mechanical simulation

Property	Value	Temperature [°C]	Source
Yield Strength	530	-	EOS 2019b
Ultimate tensile strength	640	-	EOS 2019b
Elongation at break	0.4	-	EOS 2019b